Master's thesis

NTNU
Norwegian University of Science and Technology
Faculty of Engineering
Department of Energy and Process Engineering

Simon Dehareng

The effect of active grid turbulence on the wingtip vortices and performance of a NACA-4412

Master's thesis in Energy and Environmental Engineering
Supervisor: R. Jason Hearst, Ingrid Neunaber, Tania Bracchi
June 2023

NTNU
Norwegian University of
Science and Technology

Simon Dehareng

The effect of active grid turbulence on the wingtip vortices and performance of a NACA-4412

Master's thesis in Energy and Environmental Engineering
Supervisor: R. Jason Hearst, Ingrid Neunaber, Tania Bracchi
June 2023

Norwegian University of Science and Technology
Faculty of Engineering
Department of Energy and Process Engineering

NTNU
Norwegian University of
Science and Technology

Abstract

The impact of freestream turbulence (FST) generated by an active turbulence grid (ATG) on the aerodynamic performance and behavior of a wingtip vortex in the near wake of a NACA-4412 airfoil was investigated using various experimental methods. The experiments were conducted in a large-scale closed-loop wind tunnel at four different FST conditions ($T_i = 0.2\%$, $T_i = 3\%$, $T_i = 8\%$, and $T_i = 13\%$), at a chord-based Reynolds number $Re_c = 1.4 \times 10^5$ and for an angle of attack of 5°. Force balance measurements were performed to characterize the wing performance under each FST condition. Increasing FST was observed to slightly increase the maximum lift and delay the stall. Stereoscopic particle image velocimetry (SPIV) measurements were conducted at a distance of two wing chords downstream of the trailing edge. The results showed that FST enhanced the distribution of energy transport in all directions, resulting in an increase in vortex axis meandering. After conditionally averaging the fields based on the instantaneous vortex center, the increase in FST decreased the vortex strength and increased vortex diffusion. The maximum azimuthal velocity decreased with higher FST, while the core radius of the vortex shifted towards larger radii. FST also increased the meandering amplitude and the energy contained in the long-wavelength meandering motion, at the expense of the short-wavelength meandering motion. Furthermore, digital image correlation (DIC) analysis on the displacement of the wingtip revealed a potential correlation between the wing deflection and the meandering motion.

Acknowledgements

This work is the culmination of my year as an exchange student in the Department of Energy and Process Engineering at the Norwegian University of Science and Technology (NTNU) in Trondheim, as well as the final year of my Master in Aerospace Engineering at the University of Liège, Belgium. Throughout this journey, I have had the opportunity to expand my theoretical knowledge and, more significantly, develop a passion for research through the utilization of various experimental methods. I am confident that I will take great satisfaction in applying the knowledge and skills I have acquired in my future career.

First of all, I would like to express many thanks to my main supervisor, Jason R. Hearst, for his guidance and advice throughout the project. I am particularly grateful for the trust he placed in me to undertake this work. Additionally, I extend my gratitude to my co-supervisor, Ingrid Neunaber, for her extensive assistance with the experiments. She provided me with lots of insights into the working of the tools we used and offered a comprehensive understanding of wind tunnel operations. Furthermore, I am grateful to Tania Bracchi for her support in the force balance operations.

I would also like to thank Srikar Yadala and Girish Jankee, who generously dedicated their time to setting up and calibrating the PIV system. Their contributions provided me with a valuable introduction to PIV and fueled my enthusiasm for its applications. Moreover, I am thankful to Rene Kauffmann for overseeing the DIC measurements and assisting with the set-up of the PIV and DIC systems.

I also want to thank Marie Couliou for her insightful advice and expertise in this field of study. Lastly, I would like to thank the entire Experimental Fluids NTNU team, as their contribution and input during group meetings significantly helped me to progress in this project.

Simon Dehareng
Trondheim, 6 June 2023

The effect of active grid turbulence on the wingtip vortices and performance of a NACA-4412

Simon Dehareng[a]

[a]Department of Energy & Process Engineering, Norwegian University of Science & Technology, NO-7491, Trondheim, Norway

ARTICLE INFO

Keywords:
Wingtip vortex
Meandering
Wind tunnel
Hot-wire
Force balance
Stereo PIV
DIC

ABSTRACT

The impact of freestream turbulence (FST) generated by an active turbulence grid (ATG) on the aerodynamic performance and behavior of a wingtip vortex in the near wake of a NACA-4412 airfoil was investigated using various experimental methods. The experiments were conducted in a large-scale closed-loop wind tunnel at four different FST conditions ($T_i = 0.3\%$, $T_i = 3\%$, $T_i = 8\%$, and $T_i = 13\%$), at a chord-based Reynolds number $Re_c = 1.4 \times 10^5$ and for an angle of attack of 5°. Force balance measurements were performed to characterize the wing performance under each FST condition. Increasing FST was observed to slightly increase the maximum lift and delay the stall. Stereoscopic particle image velocimetry (SPIV) measurements were conducted at a distance of two wing chords downstream of the trailing edge. The results showed that FST enhanced the distribution of energy transport in all directions, resulting in an increase in vortex axis meandering. After conditionally averaging the fields based on the instantaneous vortex center, the increase in FST decreased the vortex strength and increased vortex diffusion. The maximum azimuthal velocity decreased with higher FST, while the core radius of the vortex shifted towards larger radii. FST also increased the meandering amplitude and the energy contained in the long-wavelength meandering motion, at the expense of the short-wavelength meandering motion. Furthermore, digital image correlation (DIC) analysis on the displacement of the wingtip revealed a potential correlation between the wing deflection and the meandering motion.

1. Introduction

Wingtip vortices are, by their very nature, related to the lift produced by the wing of an aircraft. This 3D effect can significantly impact the local flow and can cause large fluctuations in the aerodynamic forces, affecting energy consumption and thus fuel efficiency. They are closely linked to the reduction of 3D lift generation in favor of induced drag. Wingtip vortices also pose a risk to nearby aircraft during take-off and landing due to the powerful gusts and eddies generated in the wake, potentially causing rolling effects and damage if not avoided promptly. For this reason, the International Civil Aviation Organization (ICAO) has established separation distances between aircraft to avoid wake vortex encounters limiting airports' capacities (Gerz *et al.* (2002)). Finally, the impact of wingtip vortices on the deflection of the wing should not be ignored. This may cause structural fatigue and damage to the wing, decreasing its lifetime. Understanding the mechanisms by which wingtip vortices interact with the wing is therefore crucial to develop strategies to mitigate their effects.

Numerous experimental studies have already focused on the evolution of wingtip vortices, acknowledging their susceptibility to a multitude of factors, including freestream turbulence (FST) and Reynolds number, $Re = U_\infty c/\nu$, where U_∞ is the freestream velocity, c is the wing chord length, and ν is the kinematic viscosity. In the 1980s, Sarpkaya & Daly (1987) studied the ambient turbulence's effect on trailing vortices of a NACA-0012 towed in a water tank at a constant angle of attack, α. They showed that FST and Crow instability contributed to a faster decay of wingtip vortices. In the 1990s, Devenport *et al.* (1996) performed experiments on the wingtip vortex of a NACA-0012 half wing oriented at 5° at a Reynolds number $Re = 5.3 \times 10^5$. This allowed them to study the vortex core's structure and to define a theory to correct the mean velocity profiles by considering the meandering of the tip vortices, defined as the low-frequency random motion of the vortex axis. With this theory, they showed that the amplitude of meandering increased with distance downstream and that the vortex core in their experiment was laminar. Chow *et al.* (1997) made near-wake measurements (up to $x/c = 0.678$ downstream of the trailing edge) of a wingtip vortex on a rectangular NACA-0012 half-wing oriented at $\alpha = 10°$ at $Re = 4.6 \times 10^6$ and at a maximum background turbulence intensity T_i of 0.15%. In

ORCID(s):

this work, $\overline{u}$ represents a time-averaged velocity, u' represents the velocity fluctuations, and $T_i \equiv \left(\overline{u'^2}\right)^{1/2} / \overline{u}$. In this w. The authors used a seven-hole pressure probe to determine the velocity field surrounding the wingtip and showed that a large axial velocity up to $1.77U_\infty$ developed in the core. They found that the turbulence decayed quickly with streamwise distance. The Reynolds stress tensor components were measured using a triple-wire probe and correlation measurements showed that the variations in the vortex position over time had a negligible impact on the measurements of turbulence properties. Heyes *et al.* (2004) evaluated the meandering of wingtip vortices using planar PIV on two NACA-0012 models ($Re = 1.0 \times 10^5$ and $Re = 2.2 \times 10^5$ respectively) oriented at 4°, 6°, 8° and 10° and mounted vertically in a wind tunnel. The background turbulence intensity in the clean wind tunnel was about 1%. In the first part, the data sets were taken at a streamwise position of $x/c = 22.9$ and were used to show the relationship between meandering amplitude and vortex strength. In the second part, data sets were taken at different streamwise positions (from $x/c = 1$ to $x/c = 23$) and the results showed that the meandering amplitude increased linearly with streamwise distance (in agreement with Devenport *et al.* (1996)) and with FST, but decreased with vortex strength.

Other research focused on the interaction of FST with the wing trailing vortices: Bailey *et al.* (2006) conducted a study on a NACA-0012 profile and showed that the FST can reduced the curvature of the wake roll-up behind the wing. The airfoil had an angle of attack of 5° for the main test and the measurements were performed at $Re = 2.4 \times 10^5$ for three FST conditions, a no-grid case ($T_i = 0.4\%$), a small grid case ($T_i = 2.5\%$) and a final large grid case ($T_i = 5\%$) at 6 transverse planes ($x/c = 0.8, 1.75, 3.75, 5.75, 7.75, 9.75$ from the quarter chord). This study showed that the tangential velocity profiles were affected by vortex meandering and that the vortex strength decreased when the FST was increased. Later, Bailey & Tavoularis (2008) measured the velocity field of a wingtip vortex performing hot-wire measurements on the same set-up and found that increasing the FST increased not only the rate of decay of the circumferential velocity but also the meandering of the vortex axis, while the radial velocity remained the same. Their results are in agreement with Chow *et al.* (1997) and Heyes *et al.* (2004).

The design of the wingtip plays a crucial role in determining the formation and characteristics of wing tip vortices. This explains why winglets are often installed on aircraft wings and why there is ongoing research into the implementation of bladelets on wind turbine blades, as discussed in the study by Reddy *et al.* (2019). The study of Giuni & Green (2013) showed the influence of the wingtip shape through smoke visualizations and SPIV measurements describing the vorticity, the axial velocity field, and the kinetic energy distribution of the vortex during its formation and in its early wake. The set-up consisted of two NACA-0012 wings, one with a squared tip and one with a rounded tip, placed in a wind tunnel. For the smoke visualization method, the two wings were tested at an angle of attack $\alpha = 12°$ and at $Re = 3000$. For the SPIV method, the wings were tested at $Re = 7.4 \times 10^5$ at $\alpha = 0°, 4°, 12°$. Four transverse planes were investigated from the leading edge, $x/c = 0.5, 0.75, 1.25, 2$. This study showed that the square-tip wing produced highly unsteady secondary vortices whose interaction with the primary vortex was the main source of meandering. The authors also identified the rolling-up of the vorticity sheet as a second cause of vortex meandering. Serrano-Aguilera *et al.* (2016) experimentally characterized the wingtip vortices in the near-field using smoke flow visualization. The set-up consisted of a NACA-0012 oriented at $\alpha = 10°$ at $Re = 3.33 \times 10^4$ and $Re = 1.0 \times 10^5$ for a maximum background turbulence intensity of 3%. The results were calculated on six different control planes from the trailing edge, $x/c = 0, 1, 2, 3, 4, 5$. They adopted the Batchelor vortex model and found that the values of the vortex strength were in good agreement with those collected in del Pino *et al.* (2011). They also showed that the Reynolds number has a small influence on the parameters of the Batchelor vortex model in the near field.

Ahmadi-Baloutaki *et al.* (2014) performed a frequency analysis of a trailing vortex flow subjected to external turbulence on a NACA-0015 wing. The study was performed in a wind tunnel at $Re = 1.6 \times 10^5$ at two FST levels (0.5% and 4.6%) and at four streamwise locations ($x/c = 0.1, 0.42, 0.77, 1.03$ from the trailing edge). The wing was oriented at an angle of attack of 10°, the velocity field was measured with a 2D hot-wire probe, and the lift and drag force were quantified via a 6-component load cell. This study demonstrated how increasing FST delays the stall, increases lift, and increases drag. The authors also demonstrated a correlation between the rise in aerodynamic forces and the rise in turbulent kinetic energy in the flow field with FST. Ghimire & Bailey (2017) performed PIV measurements to study the decay of wingtip vortices by towing a NACA-0012 wing in a towing tank. The tests were carried out for an angle of attack of 8°, and a Reynolds number $Re = 1.2 \times 10^4$. The results again showed that increasing the FST leads to a faster decay of the vortex strength, a faster decay of the peak tangential velocity, and a faster breakdown of the vortex. A year later, Bailey *et al.* (2018) investigated the vortex meandering in the turbulent near field of a NACA-0012 half-wing, showing that the meandering amplitude and the vortex core radius scaled with FST.

Table 1
Summary of experimental set-ups for some of the previous studies studying the structure and behavior of wingtip vortices. All these studies were done in wind tunnel or towing tank.

Study	Airfoil	Method	Re_c [$\times 10^5$]	T_i [%]	α [°]	x/c (origin)
Devenport *et al.* (1996)	NACA-0012	HWA	5.30	0.10	5	5, 10, 15, 20, 25 (LE)
Chow *et al.* (1997)	NACA-0012	HWA	46.0	0.15	10	[−1.14 : 0.678] (TE)
Heyes *et al.* (2004)	NACA-0012	PIV	1.00 & 2.20	1	4, 6, 8, 10	22.9 (TE)
Bailey *et al.* (2006)	NACA-0012	HWA	2.40	0.4, 2.5, 5	5	0.8, 1.75, 3.75, 5.75, 7.75, 9.75 ($c/4$)
Giuni & Green (2013)	NACA-0012	SPIV	7.40	0.4	0, 4, 12	0.5, 0.75, 1.25, 2 (LE)
Serrano-Aguilera *et al.* (2016)	NACA-0012	PIV	0.33 & 1.00	3	10	0, 1, 2, 3, 4, 5 (TE)
Ghimire & Bailey (2017)	NACA-0012	PIV	0.12	0.4, 2.5, 5	8	[0 : 2] ($c/4$)
Ben Miloud *et al.* (2020)	NACA-0012	HWA and SPIV	2.00 & 3.00	0.5, 3, 6	5	1.25, 3.25, 6.25, 7.25 ($c/4$)
Kay *et al.* (2020)	NACA-4412	Pressure taps	0.5 to 2	1.3 to 15	−6 to 20	/
Cruz Marquez *et al.* (2021*a*)	NACA-0012	SPIV	1.00	/	5	up to 60 wing-span downstream
Cruz Marquez *et al.* (2021*b*)	NACA-4412	SPIV	0.84 to 4.40	/	1 to 5.5	up to 170 wing-span downstream
Bölle *et al.* (2023)	NACA-0012	SPIV	1.70	0.5	9	2, 4, 12, 20, 26 (TE)

More recently, Ben Miloud *et al.* (2020) conducted hot-wire and stereo image particle velocimetry (SPIV) measurements in the near and mid-wake regions of a NACA-0012 ($x/c = 1.25, 3.25, 6.25, 7.75$ from the quarter chord) oriented at 5° at different T_i (0.5%, 3%, and 6%) and at $Re = 2.0\times10^5$ and $Re = 3.0\times10^5$. The authors showed that the vortex meandering amplitude and the rate of decay of the wingtip vortex increased with FST, while the vortex strength decreased with FST. Finally, they found that the vortex development was nearly independent of the Re and the FST, as there was little variation in the vortex radius and peak vorticity levels for an increasing Re. Cruz Marquez *et al.* (2021*a*) investigated the impact of a trailing edge undulation on the vortex wake of a NACA-0012 wing in a towing tank facility at $Re = 1.0\times10^5$. The waviness of the wing's trailing edge was found to have no effect on the lift or circulation, but on the radius of the vortex core and the maximum tangential velocity. The study showed that the higher the amplitude of the undulation, the larger the core radius and the lower the maximum tangential velocity. By processing the data with SPIV, they were able to identify the radial velocity profile which was in this case closest to the theoretical model of Moore *et al.* (1973). Bölle *et al.* (2023) performed PIV measurements of a jet-vortex interaction on a NACA-0012 at $Re = 1.7\times10^5$ and showed that the jet-vortex configuration followed the Moore-Saffman model, while a non-disturbed configuration fitted the Batchelor model better. Cruz Marquez *et al.* (2021*b*) studied the influence of a given span load on the vortex structure and its dynamics. The experiment consisted in towing a NACA-4412 wing at different angles of attack between 1° and 5.5° and for Re ranging from 8.4×10^4 to 4.4×10^5. SPIV measurements in different control planes in the wake showed that for high angles of attack, the axial flow deficit increased. The authors also showed that the swirling number decreased accordingly but stagnated at an constant threshold. Under similar loading conditions, an increase in the angle of attack increased the circulation, the core size, and the axial velocity of the vortex. The experimental set-ups for some of the previous investigations are summarized in Table 1.

One of the objectives of this work is to evaluate the aerodynamic behavior of an aeroelastic NACA-4412 airfoil under different turbulent inflow conditions. The effect of FST has already been examined for various types of airfoils. Li & Hearst (2021) tested an NREL S826 airfoil in a wind tunnel at a $Re = 4.0\times10^5$ and at FST varying between 0.4% and 5.4%. In this study, the authors showed that the maximum lift increased while the stall angle remained the same when the FST increased. In addition, they also identified an increase in the lift slope as T_i increased. Mueller *et al.* (1983) performed hot wire measurements in a wind tunnel to study the influence of FST on the lift and drag performance of the Lissaman 7769 airfoil. Hoffmann (1991) obtained drag and lift characteristics for the NACA-0015 airfoil at $Re = 2.5\times10^5$ and for FST ranging from 0.25% to 0.9%. Swalwell *et al.* (2001) studied the effect of FST on the stall of a NACA-0021. More recently, Kay *et al.* (2020) compared the influence of turbulence on two types of airfoils: a symmetrical NACA-0012 and a cambered NACA-4412. The study was carried out for Reynolds numbers ranging from 5.0×10^4 to 2.0×10^5 and for T_i ranging from 1.3 to 15%. The tests were conducted using pressure taps on the airfoil for angles of attack ranging from −6° to +20° in 2° steps. The main results of this study showed that for an increasing FST, the maximum lift coefficient of the cambered airfoil decreased by about 30% at $T_i = 15\%$, while for the symmetric airfoil, it increased by about 5% at $T_i = 5\%$ with respect to $T_i = 1.3\%$. Similarly, as the turbulence

intensity increased, the influence of the Reynolds number decreased. The lift coefficient of each airfoil was found to be more sensitive to Reynolds number than camber or FST.

The production of wingtip vortices has been widely investigated numerically in addition to analytical and experimental studies. These methods complete each other to provide a comprehensive understanding of the phenomenon. Dacles-Mariani *et al.* (1997) performed a comparison between a numerical and experimental study in the near field of a wingtip vortex. For the computational fluid dynamics (CFD) analysis, the computational domain was a rectangular square tip NACA-0012 wing at $\alpha = 10°$ and $Re = 4.6 \times 10^6$. They used a 3D incompressible Navier-Stokes solver, INS3D-UP (Rogers *et al.* (1991)), and a modified Baldwin-Barth turbulence model (Baldwin & Barth (1991)). For the experimental part, the measurements were performed on a similar set-up with a maximum background turbulence intensity in the wind tunnel of 0.15%. Spall (2001) brought a numerical study of a wingtip vortex applying the Euler equations for the flow over a NACA-0012 rectangular wing oriented at $\alpha = 5°$. After comparison with the experimental data, the study showed that the vortex strength and core radius were well preserved at a distance of 10 chords downstream. Craft *et al.* (2005) solved RANS equations via the UMIST's in-house code STREAM (Lien & Leschziner (1994)) to simulate the rolling-up and the development of a wingtip vortex on a NACA-0012. In this study, a comparison between different closure models was made and the main characteristics of the development of the vortex such as the core velocity and the Reynolds stresses were highlighted. More recently, O'Regan *et al.* (2013) compared the results obtained in numerical and experimental investigations of wingtip vortices near-field. The research was conducted on a square tip NACA-0012 wing at $Re = 3.2 \times 10^5$ and $\alpha = 5°, 10°$. They used a Reynolds stress turbulence model for the numerical computation and found that both data sets were in good agreement.

As a result of its major influence on aircraft performance and fuel efficiency, the evolution of wingtip vortices continues to be a topic of active investigation. One of the challenges in studying wingtip vortices in turbulent flows is the study of the vortex axis meandering and the vortex statistics. The advancements in current measurement techniques have enabled increasingly detailed investigations into this phenomenon, thereby increasing the knowledge on this subject. However, despite extensive research over the years, there are still undiscovered aspects. One particular area that has received limited attention in the literature is the potential relationship between the vortex meandering and wing deflection. It is indeed quite intuitive to conjecture that the deflection of the wing caused by FST can have an impact on the meandering characteristics of the wingtip vortex. The objective of this study is to examine the statistical properties and dynamic behavior of a wingtip vortex in the near wake of a generic aeroelastic NACA-4412 airfoil under low and high FST conditions using an active turbulence grid (ATG). The research also aims to quantify the influence of FST on the aerodynamic performance of the wing and explore the potential relationship between wing deflection and vortex meandering. This study is structured to address the following key points:

(i) Characterization of the incoming turbulence cases in the large-scale wind tunnel at the Norwegian University of Science and Technology (NTNU) using single-wire anemometry,
(ii) Force balance measurements to identify the effect of different inflow conditions on the aerodynamic performance of the wing,
(iii) Digital Image Correlation (DIC) measurements to analyze the deformation of the wing under FST,
(iv) Quantification of the flow field using Stereoscopic Particle Image Velocimetry (SPIV) measurements,
(v) Investigation of the meandering of the vortex axis and the correlation with the wing deflection.

2. Experimental set-up

2.1. Wind tunnel facility

The experiments were conducted in the large-scale closed-loop wind tunnel in the Department of Energy and Process Engineering at the Norwegian University of Science and Technology (Trondheim, Norway). The wind tunnel has a test section with dimensions of 2.71 m × 1.8 m × 11 m (width × height × length). A 220 kW fan with adjustable rotation speed placed downstream the test section drives the wind tunnel. To obtain an approximately zero-pressure gradient potential core, the roof panels could also be adjusted. Screens located upstream and downstream of the test section ensured flow quality. The wind tunnel could achieve a maximum speed of 23 m/s, and velocity measurements were taken using a Pitot tube located close to the wing for force balance measurements[1] and at various locations during the characterization of the flow. The experiments were conducted at a velocity 7.8 m/s, corresponding to a chord-based

[1]The Pitot tube was located at a sufficient distance from the wing to ensure that the measured values were not influenced by alterations in the streamlines around the wing that arise from variations of the angle of attack.

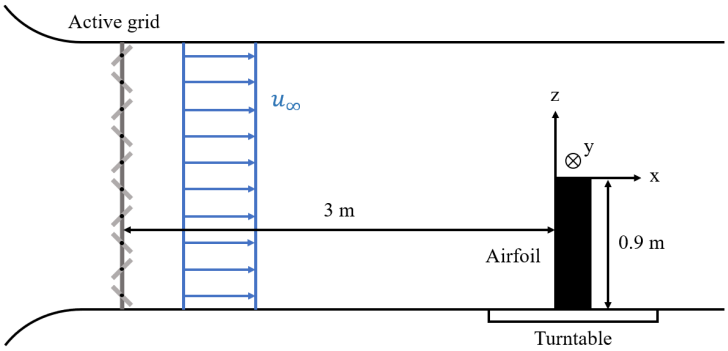

Figure 1: Schematic of the experimental set-up.

Reynolds number $Re_c = 1.4 \times 10^5$. Temperature measurements were taken using a thermocouple. The atmospheric pressure was measured at the beginning of each case using a mercury barometer.

The model used for this work is a rectangular square-tipped half-wing with a NACA-4412 profile. The airfoil was cut out of a block of polyurethane (Ebaboard 0600) which is a isotropic material with well-known characteristics and properties. The wing's surface was hand-sanded to ensure aerodynamic smoothness. The airfoil was mounted vertically in the wind tunnel test section and centered on a force balance, which could be rotated to vary the angle of attack. The rotation axis of the force balance passed through the mid-chord of the airfoil. The wing was screwed to the force balance to keep it as stable as possible while still allowing it to vibrate due to the flow. The platform of the force balance was lower than the test section floor, so a wooden plate was used to cover the mounting set-up. A gap of 4 mm was left between the plate and the airfoil so that vibrations of the airfoil did not influence the force measurements. The origin of the coordinate system was located at the tip of the airfoil $12c$, or $30M$, downstream of the test section inlet, where $c = 0.25$ m is the chord length of the airfoil and $M = 0.1$ m is the mesh length of the active grid. The x, y, and z axes were aligned with the streamwise, transverse, and spanwise directions of the wind tunnel reference frame, respectively. The distance between the coordinate system center and the mid-chord is $c/2$ so that the wing's leading edge was at the center of the coordinate system when $\alpha = 0°$. The wing had a half-span of $b = 0.9$ m and thus an aspect ratio of 7.2. A schematic of the experimental set-up is illustrated in Figure 1.

The active turbulence grid (Kildal *et al.* (2020)) used in the wind tunnel experiments enabled the generation of highly turbulent flows with the possibility of adjusting the turbulence intensity by modifying the rotational frequency of the shafts. The ATG spanned the entirety of the test section's cross-sectional area and comprised of 90 shaft assemblies, with each assembly being individually operated by a dedicated integrated stepper motor. The assemblies consisted of a stainless steel shaft with a diameter of 12.7 mm and a distance between shafts of 0.1 m denoted by M. Winglets with a diagonal length of 100 mm and a side length of 69 mm were mounted on each shaft in a diagonal arrangement next to one another. This configuration ensured maximum blockage when all the winglets were perpendicular to the flow and mimicked a static grid when the winglets were parallel to the flow.

The wing was tested at four inflow conditions at an angle of attack of 5°. The first test condition was a low turbulence reference case without any grid (REF). In the second test case, an ATG was used in static mode[2] (A). In the last two cases of the experiment, the ATG was operated in two modes to generate approximately homogeneous, isotropic turbulence. The two modes were characterized by randomized acceleration, periods of rotation, and a rotational velocity of $\Omega \pm \omega$, where ω was a random frequency as proposed by Hearst & Lavoie (2015). The third case involved spinning all the vertical axes of the active grid at a frequency of 7 ± 2 Hz (B), while in the last case, both the horizontal and vertical axes were spun at a frequency of 5 ± 2 Hz (C).

2.2. Hot-wire measurements

Hot-wire anemometry was used to measure turbulence statistics and flow homogeneity in wind tunnel without the wing model. A Dantec 55P11 single hot-wire probe, controlled by a Dantec StreamLine Pro anemometer, was employed with an offset of 1.8 and a gain of 16 to increase the signal-to-noise ratio of the measured data. The probe

[2]The active grid's motors were powered in this case to ensure that the axes maintain their homing location despite the flow in order to prevent unexpected blockage.

consisted of a tungsten sensing element with dimensions of 1.25 mm in length and 5 μm in diameter. The hot-wire employed in this study was electrically heated above room temperature. As the fluid passed in close proximity to the wire, its temperature decreased, resulting in a change in the wire's electrical resistance. This resistance change was used to determine the fluid velocity using the correction method for constant temperature and constant current anemometers, as detailed in the work of Hultmark & Smits (2010). The constant temperature mode of operation has been used. The true velocity U/ν was defined as a function of $E^2\nu/k\Delta T$, knowing the voltage E, the kinematic viscosity ν, the thermal conductivity of air k and the difference ΔT between the wire and the ambient temperatures. To measure the turbulence statistics in the wing region, the probe was fixed in close proximity to a Pitot tube and a temperature probe on the wind tunnel traverse which was controlled using a *Matlab* script. The traverse had three degrees of freedom, allowing the probe to be adjusted in the streamwise, spanwise, and vertical directions. To minimize the effect of vibrations induced by the airflow, a foot could be lowered to stabilize the traverse in a fixed position. The sampling rate was 75 kHz, with a cutoff frequency of 30 kHz for the internal anemometer low-pass filter. The overheat ratio used to adjust the wire sensitivity was set to 0.8. During the post-processing of the data, a seven-order low-pass Butterworth filter was applied to the time series at $1.1f_\eta$, where f_η is the Kolmogorov frequency. Before and after each test case, the hot-wire probe was calibrated by measuring the voltage as a function of the flow velocity on the centerline $80M$ downstream. The calibration was performed for 11 velocities. The primary properties in the wind tunnel were assessed by measuring the airflow for a duration of 600 seconds at the centerline and at a distance of $30M$ downstream, except for the REF case, which had a data collection period of 120 seconds. The homogeneity of the flow in the wind tunnel was assessed by measuring velocity time series at a total of 14 points in the wing region for 60 s each. Using the method described by Benedict & Gould (1996), the maximum random error in the turbulence intensity measurement across the 14 points and the four different cases was determined to be approximately 1.5%. The data points for the homogeneity assessment were acquired by the probe at multiple locations moving the traverse. Firstly, the traverse was moved to have the hot-wire $28M$ downstream of the flow inlet on the wind tunnel's centerline. Subsequently, the probe moved an additional $2M$ downstream to reach $30M$ corresponding to the wing's leading edge when the angle of attack is 0°. At this position, the traverse moved within the yz-plane to get data at 9 additional points on a $4M \times 4M$ grid with the central point crossed by the centerline. Thereafter the traverse proceeded to acquire data at five more positions farther downstream on the centerline, with each position being separated by a distance of $2M$.

2.3. Force measurements

To accurately measure the forces acting on the wing, a six-component force balance produced by Carl Schenck AG was used. The design of the force balance incorporated the mounting of the six load cells onto the rotating platform, which enabled the load cells to rotate simultaneously with the wing whilst changing the angle of attack. The first three load cells were designed to measure the vertical force components, while the remaining three were specifically designed to measure the horizontal force components. The three horizontal load cells were used to determine the lift and drag components. Before performing any force measurements, a load cell calibration was conducted using a known weight standard. The output voltage was recorded for various known weights, and a linear relationship between the load cell output and the weights was established through linear interpolation. For calibration measurements, the sampling rate was set to 2000 Hz, and the sampling time was 10 s.

Measurements were taken for angles of attack ranging from $-5°$ to $+25°$. A LabView program was used to acquire voltage readings for each load cell and from the thermocouple and Pitot tube. During an initial test, hysteresis was observed. The offset drifted, requiring frequent offset measurements in the subsequent measurements. The voltage offsets obtained from interpolation between the offsets measured before and after each lift curve measurement were subtracted from the voltage obtained for the lift curve. For the low-turbulence case and the ATG static case, one 4-minute sample at a sampling frequency of 2000 Hz was taken for each angle of attack. In order to obtain converging results for the two most turbulent cases using the ATG and given the limited capacity of the program used, three 3-minute samples at a sampling frequency of 2000 Hz were taken and then averaged for each angle of attack.

2.4. SPIV measurements

2D-3C Stereoscopic Particle Image Velocimetry (SPIV) measurements were conducted to measure the three components of the instantaneous velocity field in the wake of the wing at an angle of attack of 5°. The airflow was seeded with Di-Ethyl-Hexyl-Sebacate (DEHS) particles of approximately 1 μm in diameter. The particles were illuminated with a Nd:YLF Litron LDY303HE high repetition rate laser (diode-pumped, dual cavity, laser system) emitting green light at a wavelength of 527 nm. The maximum pulse energy was 28 mJ. A first acquisition protocol at 200 Hz was used

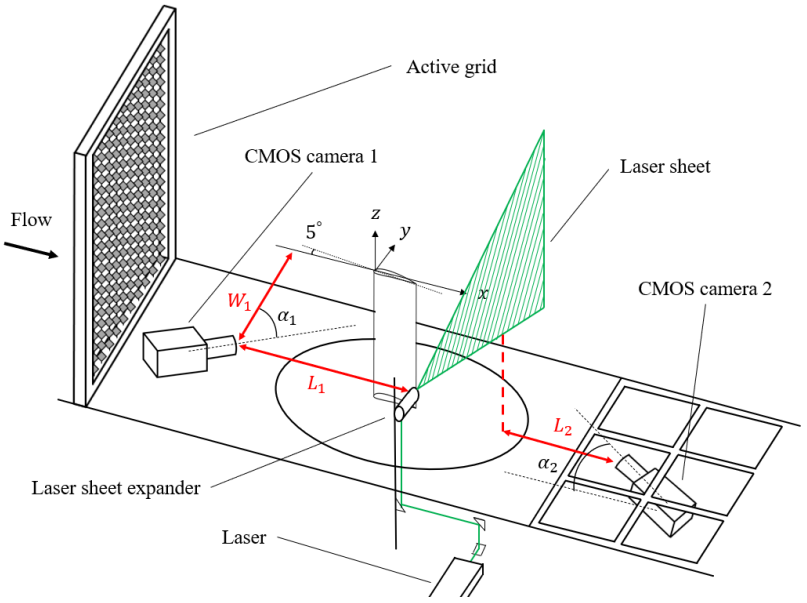

Figure 2: Schematic of the stereo-PIV set-up. The first CMOS camera was located on the side of the wind tunnel and was pointing towards the upstream face of the laser sheet while the second camera was located under the wind tunnel and was tilted upwards to point towards the downstream face of the laser sheet. The schematic is not to scale.

to capture flow statistics and a second one at 2000 Hz was used to capture flow dynamics. Moreover, two 2000 Hz series were acquired for each turbulence case to ensure that the perceived results were not idiosyncratic. Data acquisition was conducted for 50 s in the low-speed protocol and for 5 s in the high-speed protocols, resulting in a total of 10 000 images being recorded for each case. The images were captured in double-frame mode, with a pulse separation of 100 μs between two high-speed PIV images and 1 ms between two low-speed PIV images. To prevent any interference from the laser light, a delay of 200 μs for the high-speed case and 2 ms for the low-speed case was introduced between the high-speed PIV and DIC measurements.

Figure 2 shows the SPIV experimental set-up. The laser beam was reoriented through reflective mirrors before being directed through sheet optics to create the laser sheet. The imaging was carried out using two high-speed *Phantom v2012* cameras equipped with a 1280 px × 800 px CMOS sensor (pixel pitch of 28 μm). The camera lenses used for the experiment was a *Nikon* 200 mm-Micro lens for PIV adjusted to a numerical aperture of $f_\# = 5.6$, and the focal length was 200 mm. The first camera was located on the side of the wind tunnel, 1500 mm from the centerline in the transverse direction (W_1), 1300 mm from the laser sheet in the streamwise direction (L_1), and directed towards the upstream side of the measurement plane at an angle $\alpha_1 \approx 40°$. The second camera was placed on the centerline beneath the wind tunnel, 1400 mm downstream of the plane, and tilted upward to point at an angle $\alpha_2 \approx 40°$ towards the downstream side of the measurement plane. To ensure accuracy in the measurements, a two-level calibration plate from *LaVision* was employed at the measurement plane parallel to the yz-plane. Specifically, the center of the calibration target was set $2c$ downstream of the trailing, which was already deflected at 5° angle of attack, and aligned in the spanwise direction, 2 mm above the trailing edge. This plane was chosen based on smoke visualization at different turbulence levels to see if the vortex was sufficiently developed and could be effectively studied at this distance. Figure 3a and Figure 3b show the evolution of the wingtip vortex downstream of the trailing edge for all axes of the ATG spinning at 5 ± 2 Hz, and at low speed. Furthermore, it was ensured that the calibration target center was aligned with the trailing edge of the wing. In order to coincide with the measurement plane and to ensure that both cameras capture sharp and in-focus images of the particles in the same plane, Scheimpflug adapters were used to tilt the focal plane of each camera. The *LaVision DaVis 10.2.1* software was used for the calibration, image acquisition, pre-processing, and cross-correlation. The final correlation window size to compute a single vector was 32 px × 32 px with an overlap of 50%, resulting in a vector spacing of approximately 3 mm in both y- and z-direction. Due to some lens aberrations at the edges of the window, a final window size of 54 × 54 vectors was used for data analysis. The final vector field resulted in a 160 mm × 160 mm FOV.

(a) (b)

Figure 3: (a) Smoke visualization of the wingtip vortex near the trailing edge. (b) Focus on the downstream evolution of the vortex. All axes of the ATG were spinning at 5 ± 2 Hz and the velocity was reduced to see the vortex core. Full videos showing the evolution of the vortex for the turbulence cases can be seen in the attachments to this work.

Table 2
Uncertainties in time-averaged velocity fields for low and high-speed PIV data in the different cases. The values presented correspond to the uncertainties in the mean velocity components in the streamwise, spanwise, and vertical directions ($\epsilon_{\overline{u}}$, $\epsilon_{\overline{v}}$, and $\epsilon_{\overline{w}}$). (REF) no ATG, (A) Static ATG, (B) Vertical ATG axes spinning at 7 ± 2 Hz, (C) All ATG axes spinning at 5 ± 2 Hz.

	Low-speed PIV				High-speed PIV			
	REF	A	B	C	REF	A	B	C
$\epsilon_{\overline{u}}$	0.8%	1.8%	1.8%	2.4%	11.9%	11.7%	10.7%	10.2%
$\epsilon_{\overline{v}}$	1.0%	1.5%	1.0%	1.8%	2.8%	3.4%	3.1%	3.0%
$\epsilon_{\overline{w}}$	0.6%	0.9%	1.6%	1.4%	2.3%	3.2%	3.5%	4.0%

Raffel *et al.* (2018)'s estimation of the correlation error is 0.1 px. In the current experiment, the typical particle displacement was around 10 pixels, leading to a 1% relative error in displacement measurement. The very low error in time separation between frames, the uncertainty of the magnification coefficient, and the uncertainty associated with the ability of the particles to follow the fluid were neglected. The measured velocity field, represented by the time-series of instantaneous velocity fields $u(t)$, had therefore a relative error of $\epsilon_{u(t)} = 1\%$. In this work, each PIV frame captures the velocity field for each of the velocity components. The instantaneous velocities are represented as $u = \overline{u} + u'$ for the streamwise component, $v = \overline{v} + v'$ for the transverse component, and $w = \overline{w} + w'$ for the spanwise component. The symbols u', v', w' indicate the velocity fluctuations, and each variable denoted with an overbar represents an average across all the frames. The symbol $\langle \cdot \rangle$ represents an ensemble average.

Using the linear propagation technique described in Sciacchitano & Wieneke (2016), the uncertainty $\epsilon_{\overline{u}}$ of the averaged velocity field $\overline{u}$ could be computed from the standard deviation $\sigma_{u(t)}$ of the corresponding time-series and the number of uncorrelated samples N_{eff} for high-speed PIV results and the total number of samples for low-speed PIV results. The uncertainties on the time-averaged field in the current experiment are summarized in Table 2.

2.5. DIC measurements

Digital Image Correlation (DIC) is an optical method that enables non-contact measurement of surface deformation and displacement. In this work, DIC was employed to analyze digital images captured before and after deformation in order to assess the behavior of the wingtip displacement. The experimental set-up consisted of two high-resolution *Photron* SA1.1 cameras, positioned at angles $\alpha_3 = \alpha_4 \approx 40°$ relative to the normal direction of the high-pressure side of the airfoil surface, and at a distance W_1 from it. These cameras were equipped with a 12-bit monochrome CMOS sensor with a resolution of 1024 px × 1024 px. The sensor exposure time was 199.46 μs, the pixel pitch was 20 μ, and the scale was approximately 0.3 mm/px. The cameras were equipped with *Sigma* 50-100 mm lenses, which were adjusted to a numerical aperture of $f_\# = 1.8$, and had a focal length of 100 mm. The selected FOV encompassed a 53.7 mm in height and 218.4 mm in width rectangular area located at the tip of the wing. To achieve uniform illumination across the wing

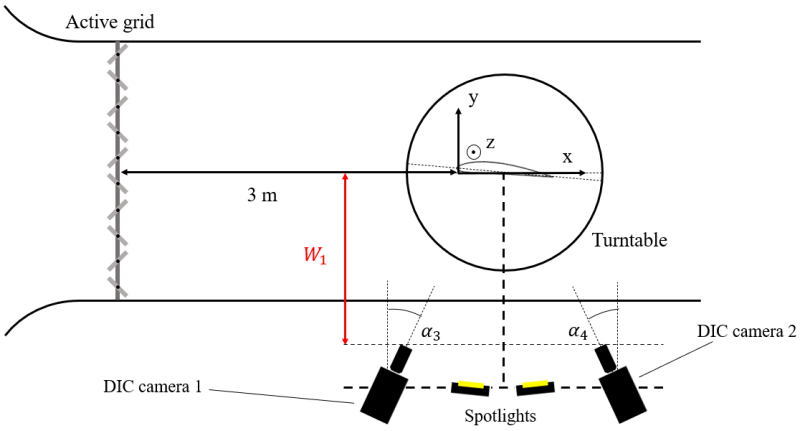

Figure 4: Schematic of the DIC set-up. The two DIC cameras were located on the side of the wind tunnel and were pointing towards the speckle pattern on the lower surface of the wing, while light sources were also pointing at the speckle pattern to provide the necessary illumination. The schematic is not to scale. Note that both SPIV and DIC set-ups were mounted together as they exhibited no interference or cross-talk with each other.

surface of interest, the set-up incorporated two GS *Vitec* LED light sources positioned at a distance W_1 from the wing, between the two DIC cameras as shown in the DIC set-up in Figure 4. Polarizers were set in front of the spotlights and cameras to reduce glare. The calibration was done via a cylinder-based stereo calibration. The displacements were tracked with a speckle pattern applied on the wing, which can be seen in Figure 3a. The speckle pattern consisted of randomly arranged points, each approximately 0.5 mm in diameter. For calibration and data acquisition, *LaVision DaVis 10.2.1* software was used. High-speed data were collected at a sampling rate of $f_s = 2000$ Hz, while low-speed data were collected at a rate of $f_s = 200$ Hz. The correlation analysis was conducted using global DIC correlation with a data mesh element size of 15. To ensure accurate correlation results and enhance image resolution, bicubic spline image interpolation and gray-level normalization techniques were employed. The post-processing was done in *Ecorr 6* and *Matlab*.

3. Flow conditions

A preliminary study of flow homogeneity in the empty wind tunnel was performed by evaluating the main turbulence characteristics under the four test conditions: the REF case without grid, the A case with the ATG in static mode, the B case with the vertical ATG axes spinning at 7 ± 2 Hz, and the C case with all ATG axes spinning at 5 ± 2 Hz. Firstly, the homogeneity was evaluated along the centerline of the wind tunnel, from a distance of $0.8c$ upstream of the leading edge to a distance of $2.2c$ downstream of the trailing edge (total distance of $10M$). The results showed that T_i remained around 0.2% in the reference case, decayed from 3% to 2.5% in the first grid case, from 8.5% to 7.8% in the second grid case, and from 13% to 11.5% for the third grid case. It must be acknowledged that this decay would be greater over longer distances. The mean velocity remained relatively constant for all test conditions, with standard deviations from the ensemble average of the mean velocities along the centerline of 0.009 m/s ($\langle\overline{u}\rangle = 7.33$ m/s), 0.009 m/s ($\langle\overline{u}\rangle = 7.73$ m/s), 0.038 m/s ($\langle\overline{u}\rangle = 7.81$ m/s), and 0.061 m/s ($\langle\overline{u}\rangle = 7.54$ m/s), respectively.

Secondly, the homogeneity was assessed at a distance $30M$ downstream, using a $4M \times 4M$ grid oriented perpendicular to the flow. The analysis array consisted of 9 points, with the central point being the second point used in the centerline homogeneity analysis meaning that the same point was used both in the centerline analysis and in the analysis of the flow farther downstream of the grid. The homogeneity in $\overline{u}$ and T_i of the flow over the $4M \times 4M$ array is shown in Figure 5. In agreement with Hearst & Lavoie (2015), the random ATG cases exhibited the highest level of homogeneity with a decrease in the variability of $\overline{u}/\overline{u}_c$ and T_i/T_{i_c}. It should be mentioned that for the second ATG case with the vertical axes spinning at 7 ± 2 Hz, the two values in the upper right corner deviate significantly from the rest. This discrepancy was attributed to the blockage brought by one of the horizontal shafts in the upper right quadrant of the ATG that did not home properly before the measurements.

Table 3 summarizes the main turbulence flow conditions measured at a distance of $30M$ downstream of the inlet on the centerline. These conditions were evaluated under the four test configurations, i.e. the reference case without

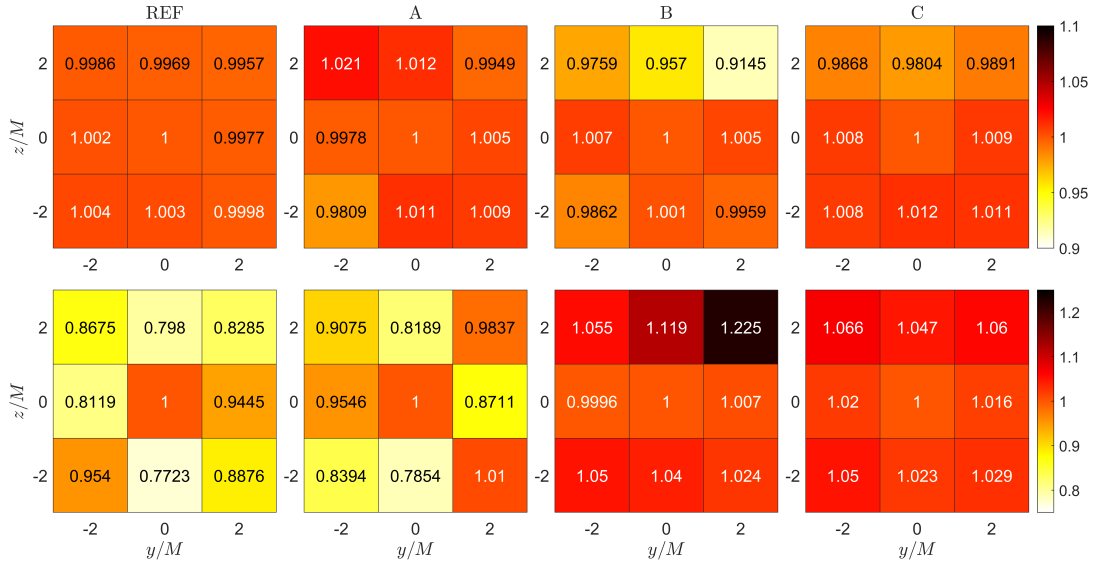

Figure 5: Homogeneity of the flow for a $4M \times 4M$ array $30M$ downstream. The values for $\overline{u}$ (above) and T_i (below) are normalized by the centerline values. (REF) No ATG, (A) Static ATG, (B) Vertical ATG axes spinning at 7 ± 2 Hz, (C) All ATG axes spinning at 5 ± 2 Hz.

Table 3
Summary of the main characteristics in the empty wind tunnel. The turbulence properties were taken at $30M$ downstream of the wind tunnel inlet. The isotropy ratios were computed using PIV measurements for the empty wind tunnel at a distance of $37.5M$ downstream. (REF) no ATG, (A) Static ATG, (B) Vertical ATG axes spinning at 7 ± 2 Hz, (C) All ATG axes spinning at 5 ± 2 Hz.

Inflow case	$\Omega \pm \omega$ [Hz]	$\overline{u}$ [m/s]	L_{ux}/M	$u'/\overline{u}$ [%]	Re_λ	u'/v'	u'/w'
REF	/	7.34	/	0.23	/	0.98	1.31
A	/	8.47	0.15	2.93	77	1.22	1.46
B	7 ± 2	7.77	0.58	8.22	300	1.03	1.26
C	5 ± 2	7.85	0.73	13.34	429	1.01	1.06

ATG, the ATG static mode, the first random ATG case (7 ± 2 Hz, vertical axes spinning), and the second random ATG case (5 ± 2 Hz, all axes spinning). The table includes values for the mean velocity, the turbulence intensity, the integral length scale, the Taylor microscale-based Reynolds number, and the isotropy ratio. The latter was measured by ensemble-averaging the isotropy ratios over the whole relevant window for data analysis in SPIV measurements. It is worth noting that the random ATG cases exhibit greater isotropy in the flow compared to the static ATG case and the no-ATG case, as predicted in Hearst & Lavoie (2015).

The energy spectra obtained from the hot-wire measurements for the three ATG cases are shown in Figure 6. The frequency and power axis were plotted on a logarithmic scale and non-dimensionalized with η, as the Kolmogorov length, κ, as the wavenumber, and ν, as the kinematic viscosity. The $(\kappa\eta)^{-5/3}$ black line represents the $-5/3$ exponential decay for the inertial range of a homogeneous, isotropic flow. The absence of low-frequency peaks in the spectra indicates that the active grid forcing does not preferentially energize a particular frequency or set of frequencies. However, some differences in the inertial subrange and the energy distribution for the lowest frequencies between the three cases should be noted. In particular, and in agreement with Larssen & Devenport (2011), the random ATG cases had a larger inertial subrange, suggesting a greater range of scales in the flow. Additionally, the energy contained in the flow for low frequencies is greater in the most turbulent cases, indicating an increase in kinetic energy in the flow.

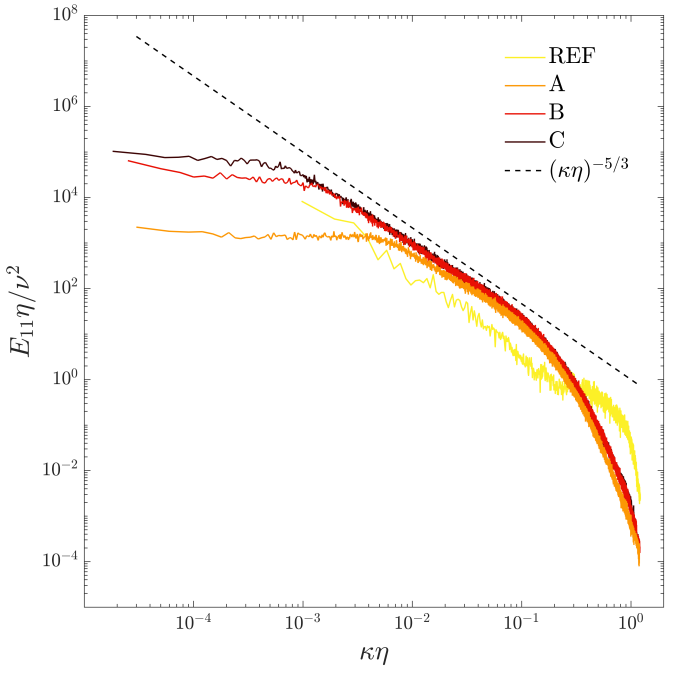

Figure 6: Energy spectra of hot-wire measurements for the three active grid cases. The spectra exhibit a clear trend towards increasing energy at lower frequencies, with the highest turbulent case showing the greatest energy content at low frequencies. (REF) $T_i = 0.2\%$ (A) $T_i = 3\%$, (B) $T_i = 8\%$, (C) $T_i = 13\%$.

4. Forces

Figure 7 shows how the 3D lift coefficient obtained with force balance measurements varies with the angle of attack for the four test cases. The 3D lift coefficient is expressed as $C_L = L/\left(\rho_a U_\infty^2 A/2\right)$, where the lift force L was computed and averaged from voltage time series from the force balance, ρ denoted the air density in the wind tunnel, U_∞ was the local freestream velocity, and A was the reference surface area of the wing. At first glance, the slopes of the lift curves appeared to be similar in the linear range of the curve, suggesting that FST has little influence on the aerodynamic behavior of the wing in this region. However, this conclusion should require further examination, as the shape of some curves suggested some precision errors in the measurement of the linear range. There was also a slight increase in the maximum lift coefficient when increasing T_i which is consistent with the work of Li & Hearst (2021) but in opposition with the findings of Kay *et al.* (2020), who observed a decrease in the maximum 2D lift coefficient of a NACA-4412 airfoil when increasing the FST from 1.3% to 15%. From $\alpha = 15°$, the behavior of the lift curves started to differ for each case. As T_i increased, the angle at which the stall occurred shifted to larger α, indicating that turbulent fluctuations in the flow have a notable effect. This finding is consistent with several previous studies, including those by Ahmadi-Baloutaki *et al.* (2014), Swalwell *et al.* (2001), and Kay *et al.* (2020). The stall delay when increasing FST was likely attributable to the velocity fluctuations at the wing surface that energize the boundary layer, forcing it to remain attached to the wing surface for longer periods, thus reducing the likelihood of separation and stall.

Li & Hearst (2021) demonstrated an increase in the maximum 2D lift coefficient C_l of an NREL-S826 for increasing T_i, but the increase in this case seemed very small. The 3D effects may have played a role in the reduction of lift, in particular with the induced drag caused by the wingtip vortex, even though turbulence can help to break up and dissipate the vortex. The 3D effects may have balanced with the influence of FST and potentially explain the lower rate of increase in the lift coefficient. It is worth mentioning that the influence of 3D effects on the aerodynamic performance of a wing under different FST cases is not well-represented in experimental literature, and can be a promising subject for future research.

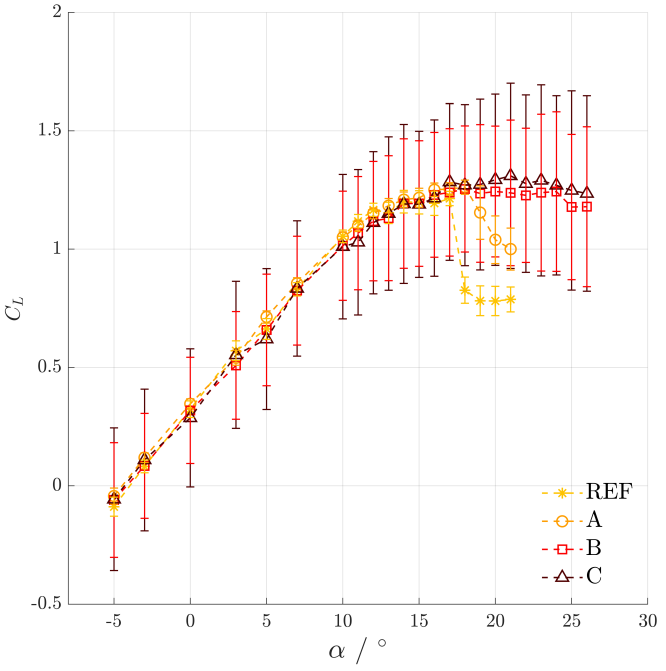

Figure 7: Impact of turbulence intensity on the lift performance of a NACA-4412 airfoil. Increasing darkness indicates increasing turbulence intensity. (REF) $T_i = 0.2\%$, (A) $T_i = 3\%$, (B) $T_i = 8\%$, (C) $T_i = 13\%$.

At lower levels of turbulence, the wing exhibited a sudden and unpredictable stall behavior characterized by a sharp drop in lift between $\alpha = 17°$ and $\alpha = 18°$. On the drag curve for the low turbulent case shown in Figure 8a, this resulted in a sudden increase in drag. As the turbulence intensity increased, the stall behavior became smoother and more predictable, with the wing gradually losing lift and increasing drag in a more controlled manner. The polar drag curves for each turbulence case are also displayed in Figure 8b. For the low-turbulent case, the drag polar curve exhibited a sharp reduction in C_L with increasing C_D, indicating a sudden onset of stall. In contrast, as T_i increased, the drag polar curves showed a more gradual decrease in C_L, suggesting a transition to a smoother stall behavior, facilitated by the turbulent flow which helped to delay airflow separation over the wing.

To account for the fluctuations caused by the turbulence, bars representing the standard deviation of the time series were added to each data point. These bars showed that an increase in T_i led to an increase in the fluctuations for both lift and drag data. This can be seen with the larger bars for higher T_i values. The observed increase in fluctuations suggests that FST has an impact on the lift coefficient. Additionally, the drag curve displayed a progressively increasing sensitivity to turbulence as a function of α, with minimal fluctuations observed when approaching $\alpha = 0°$.

5. Deflections

In this section, the analysis of the wingtip displacements under the different turbulence cases performed through DIC measurements is presented. The statistical parameters characterizing the wing motion in the y-direction are presented in Table 4. These parameters encompassed the mean displacement and standard deviation, offering valuable insights into the magnitude and the variability of the wing motion. The main observation deduced from the table values is the increase in absolute mean and in standard deviation when increasing FST. One can also notice the slight elevation in standard deviation between the leading and the trailing edge displacements, as a consequence of the reduced thickness at the trailing edge inducing a higher flexibility.

Figure 9a and Figure 9b depict the first two Proper Orthogonal Decomposition (POD) modes for wing deformation based on DIC measurements. The color scale used in the figures reflects relative values rather than absolute values, as the focus lies on the relative displacements of the wing tip points with respect to each other. The first and the

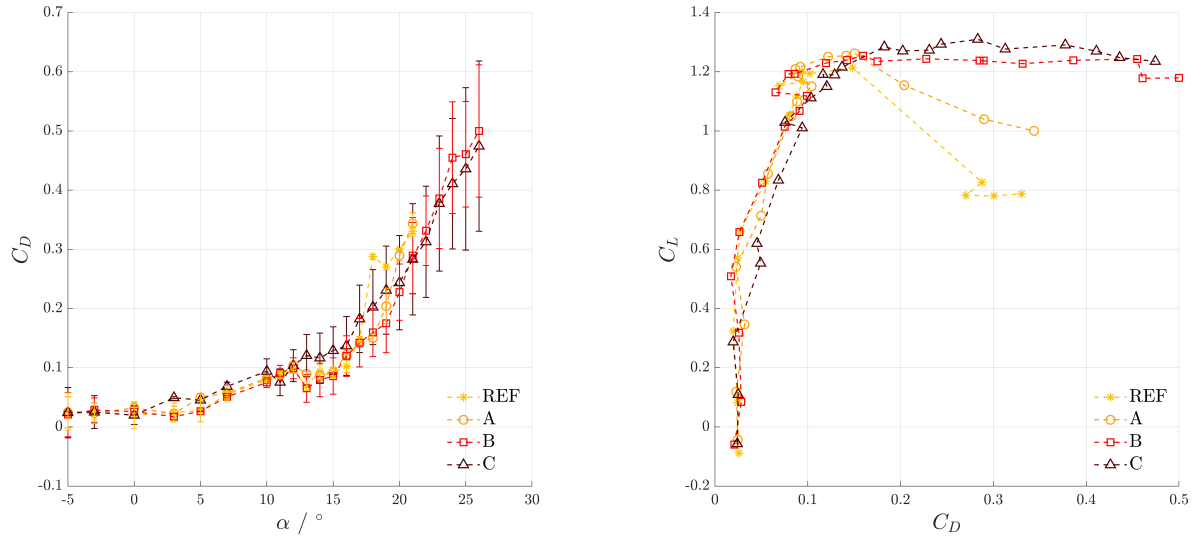

(a) (b)

Figure 8: Impact of turbulence intensity on the drag of a NACA-4412 airfoil. (a) shows the drag curves plotted against the angle of attack, while (b) displays the drag polar curves for different turbulence cases. The darkest colors indicate higher turbulence levels. (REF) $T_i = 0.2\%$, (A) $T_i = 3\%$, (B) $T_i = 8\%$, (C) $T_i = 13\%$.

Table 4
Mean and standard deviation of the wing motion in the y-direction. The statistics are taken at leading and the trailing edge, and at the tip of the wing. (REF) $T_i = 0.2\%$, (A) $T_i = 3\%$, (B) $T_i = 8\%$, (C) $T_i = 13\%$.

		Leading edge				Trailing edge			
		REF	A	B	C	REF	A	B	C
$\overline{\Delta y}$	[mm]	0.011	0.038	0.289	3.685	0.012	0.035	0.298	3.822
$\Delta y'$	[mm]	0.014	0.032	1.606	2.107	0.015	0.033	1.645	2.170

most energetic mode, displayed in Figure 9a, revealed a bending tendency along the span. This mode corresponds to the predominant vibration mode observed during the conducted experiments, where the wing primarily exhibited the behavior of a cantilever beam. In contrast, the second mode, displayed in Figure 9b, showed the wing deformation occurring between the trailing and the leading edges. The color map used for the rigid-body mode (first mode) emphasized deformations of the same sign, where decreasing darkness indicated an increase in displacement relative to the other points. Conversely, a polar color scale (red and blue) was used for the second mode to depict the presence of both positive and negative displacements, indicating a pitching deformation of the wing along the mid-chord. These are the two modes one would expect to see with the most energy, i.e. wing bending, and wing twist, and thus the turbulence does not influence these. The first two modes account for 18%, 31%, 95%, and 97% of the total energy in the POD decomposition for the respective test cases (REF, A, B, and C) as FST increases, and are therefore dominant for the most turbulent test cases.

The frequency spectra of the displacement at the tip trailing edge are presented in Figure 10. In each of the turbulence cases, a distinct energy peak was consistently observed at a frequency of 6.2 Hz. This frequency corresponds to a chord-based reduced frequency of $fc/U_\infty = 0.1987$. The fact that the peak occurred across all turbulence cases suggested that the frequency at which the wing vibrates was not a consequence of the FST generated by the ATG, in contrast to the magnitude of the displacement. To validate this assertion, a straightforward test was conducted to determine the wing's eigenfrequency. By employing a laser pointer, and a laser displacement sensor (ILD2310-50) configured at a sampling frequency of 2000 Hz and for a sampling time of 10 s, the frequency spectrum of the wing

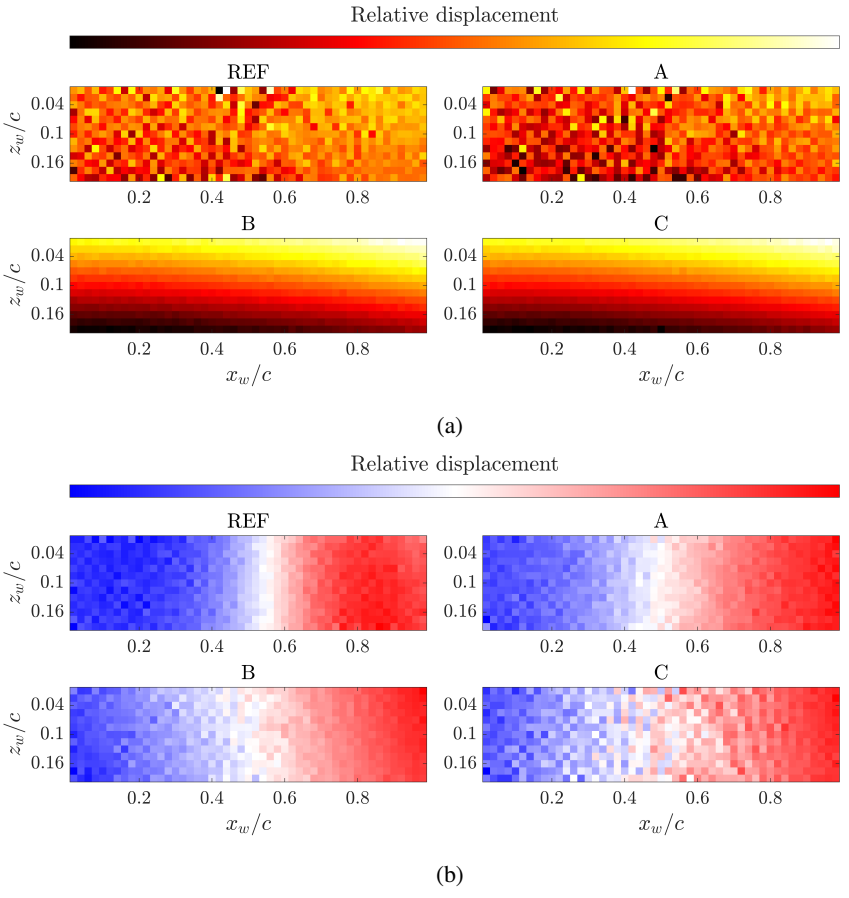

Figure 9: (a) First POD mode for the displacement along y-direction for every turbulence case. (b) Second POD mode for the displacement along y-direction for every turbulence case. (REF) $T_i = 0.2\%$, (A) $T_i = 3\%$, (B) $T_i = 8\%$, and (C) $T_i = 13\%$. The FOV represents the tip of the wing. Only the relative values are of importance. The coordinate system was set to have $z_w/c = 0$ at the tip and $x_w/c = 0$ at the leading edge of the wing.

could be analyzed after striking the wingtip along the y-direction. The frequency spectrum resulting from this test is presented in Figure 10, where the frequency peak aligns with the ones from the DIC measurements. Therefore, the observed peak corresponds to a natural frequency inherent to the structural properties of the wing.

6. Wingtip vortex statistics

This section focuses on the analysis of statistical properties extracted from the SPIV data. The quantities studied in this section were therefore mainly derived from the low-speed PIV acquisition. The mean velocity and fluctuation fields, the mean axial swirling strength, and the averaged azimuthal, radial, and axial velocity profiles were investigated. The probability distributions of the vortex characteristics were also studied.

6.1. Mean velocity fields

Figure 11a displays the contour plots for the streamwise velocity deficit $(\overline{u} - U_\infty)/U_\infty$ for the four test cases: (REF) no ATG, (A) static ATG, (B) first random ATG case, (C) most turbulent random ATG case. Although the wake deficit may not form a perfectly circular region, there was a noticeable wake increase in the wake deficit near the center of the frame, corresponding to the wake of the wing's trailing edge. The velocity deficit located in the top right corner of the window was believed to be due to the wake of the wing's leading edge. Comparing the four cases, the largest axial velocity deficit was observed for the no-grid case, while the deficit became less intense as FST increased. This conclusion is consistent with Bailey & Tavoularis (2008), Ben Miloud *et al.* (2020), and Pentelow (2014). In the left

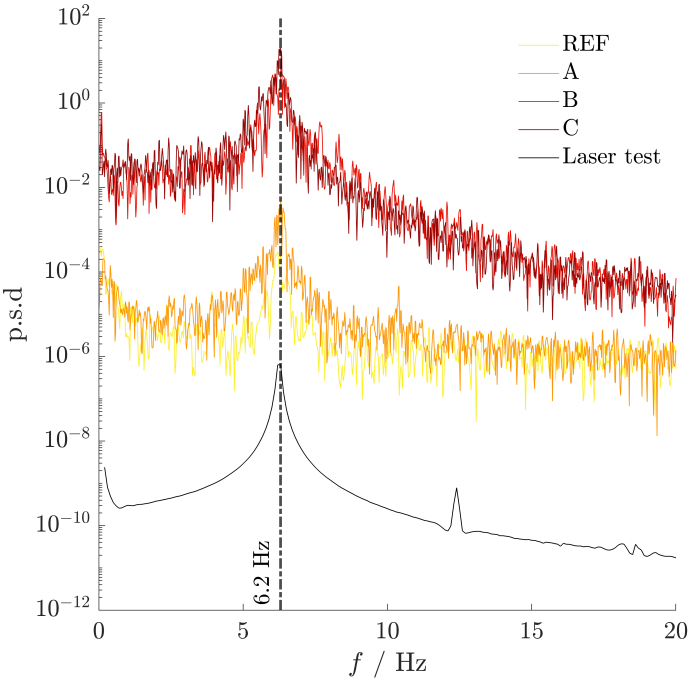

Figure 10: Frequency spectra of the wingtip trailing edge displacement for each turbulence case. The magnitude of the laser test spectrum was taken arbitrary to show the comparison with the other spectra. (REF) $T_i = 0.2\%$, (A) $T_i = 3\%$, (B) $T_i = 8\%$, and (C) $T_i = 13\%$

bottom corner, the roll-up of the wake shear layer can be identified. Similar to the behavior observed in the vortex core, the velocity deficit in the wake shear layer showed a decreasing trend as FST increased. For the most turbulent case, only the core remained, which is in agreement with the PIV measurements conducted by Pentelow (2014).

Figure 11b shows the axial rms velocity fluctuations $\left(\overline{u'^2}\right)^{1/2}$ over the local freestream streamwise velocity fluctuations $\left(\overline{u'^2_\infty}\right)^{1/2}$ for the different cases, which were more pronounced near the center of the vortex. These results are in agreement with the research by Green & Acosta (1991), and Devenport *et al.* (1996) who found that velocity fluctuations were highest in the vortex core, indicating high levels of unsteadiness. As the FST increased, the ratio of streamwise velocity fluctuations to freestream velocity fluctuations generally decreased, causing the fluctuations in the flow and especially in the vortex core to become more uniform. It is noteworthy that the axial velocity deficit and fluctuations observed in the static ATG case exhibited a non-conventional shape. This deviation from the expected behavior could be attributed to the relatively poor homogeneity provided by the static ATG mode, as indicated by the isotropy ratios in Table 3.

Figure 12a and Figure 13a display the velocity fields in the transverse and the spanwise directions, respectively. The color bars were configured so that the positive velocities were shown in red and the negative velocities in blue. By comparing the two figures, the vortex center could be identified with the polarity of the colors. The velocity fluctuations are shown in Figure 12b and Figure 13b. Like the streamwise velocity fluctuations, they were more pronounced at the vortex center, and the roll-up of the vortex sheet was also noticeable. Additionally, the normalized fluctuation became smaller as FST increased, leading to an increase in the homogeneity of the flow fluctuations in the frame. The figures also revealed an increase in the vortex size as FST increased, in agreement with Bailey *et al.* (2018), who found that the vortex size scaled with FST.

Figure 14 illustrates the evolution of the maximum velocity fluctuations for the streamwise, transverse, and spanwise directions and for the four turbulent cases. The transverse v' and the spanwise w' components exhibited higher magnitudes compared to the streamwise component, in each of the turbulence cases. According to Bölle *et al.*

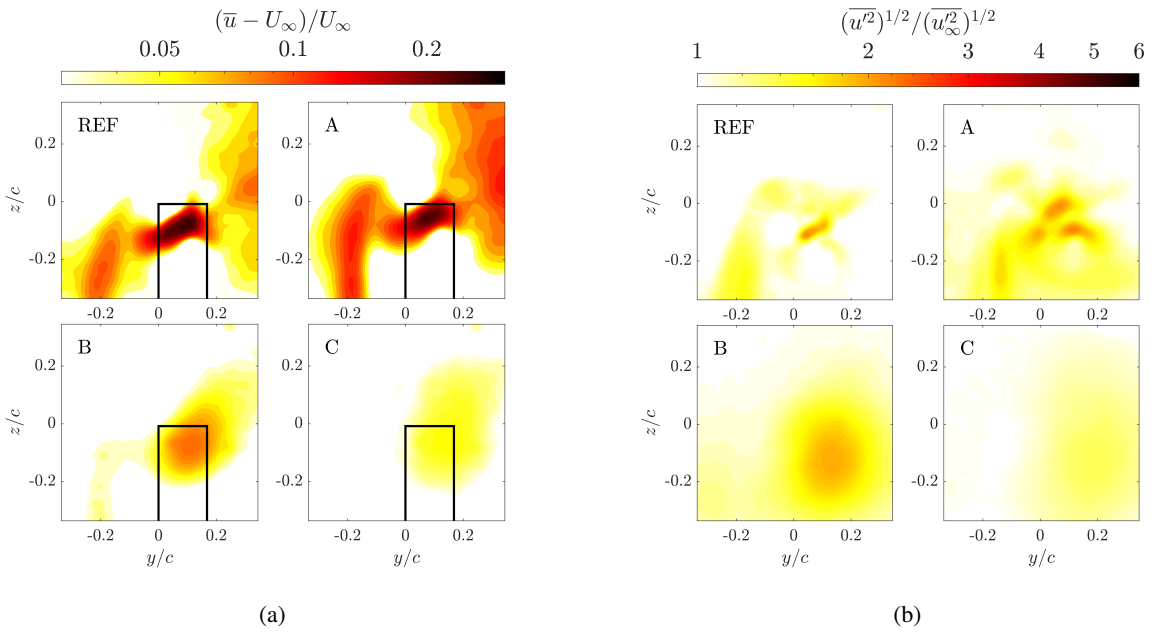

Figure 11: (a) Contours of the normalized streamwise velocity deficit. The black rectangle represents the projected area of the wing. (b) Contours of the normalized streamwise velocity fluctuations. (REF) $T_i = 0.2\%$, (A) $T_i = 3\%$, (B) $T_i = 8\%$, and (C) $T_i = 13\%$. Note that the freestream fluctuation rms value vary also with the turbulent case.

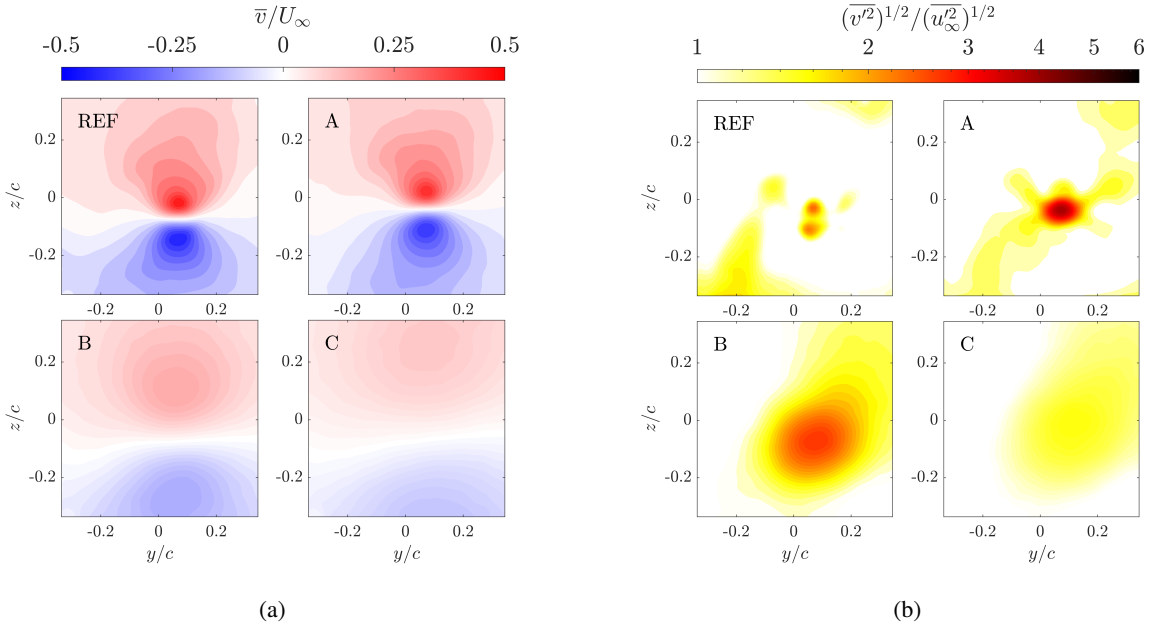

Figure 12: (a) Contours of the normalized transverse velocity field. (b) Contours of the normalized transverse velocity fluctuations. (REF) $T_i = 0.2\%$, (A) $T_i = 3\%$, (B) $T_i = 8\%$, and (C) $T_i = 13\%$. Note that the freestream fluctuation rms value vary also with the turbulent case.

(2023), this indicated that the fluctuation kinetic energy of the streamwise component $k_{xx} = \overline{u'^2}/U_\infty^2$ was lower than that of the transverse and spanwise components $k_{yy} + k_{zz} = \left(\overline{v'^2} + \overline{w'^2}\right)/U_\infty^2$. Bölle *et al.* (2023) concluded that

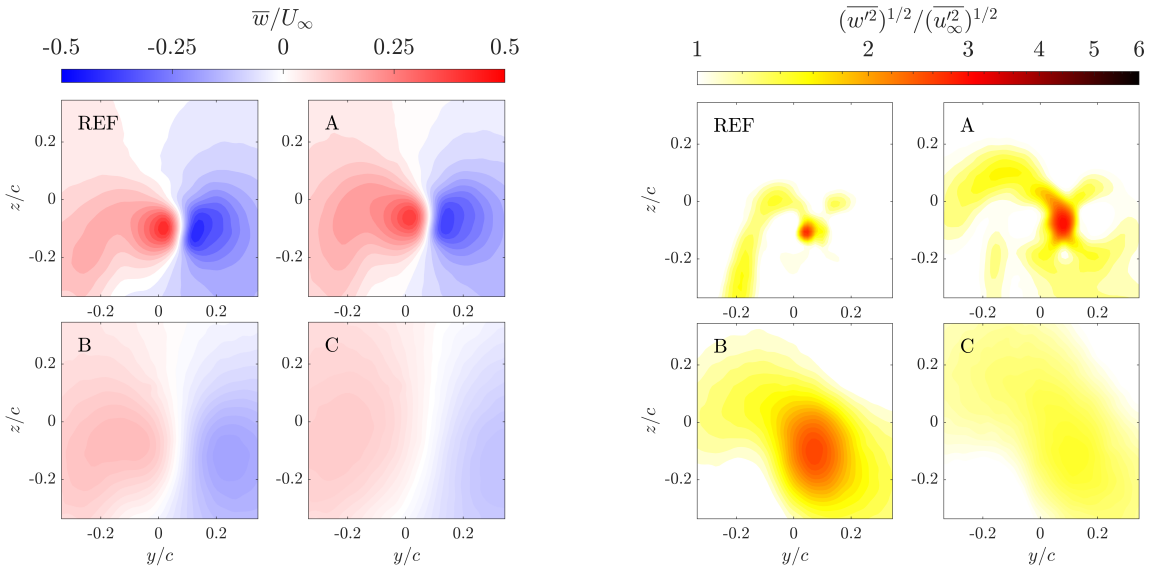

(a) (b)

Figure 13: (a) Contours of the normalized spanwise velocity field. (b) Contours of the normalized spanwise velocity fluctuations. (REF) $T_i = 0.2\%$, (A) $T_i = 3\%$, (B) $T_i = 8\%$, and (C) $T_i = 13\%$. Note that the freestream fluctuation rms value vary also with the turbulent case.

the primary vortex mode responsible for carrying energy was more closely related to transverse and spanwise motion rather than streamwise motion. Upon comparing the fluctuations for the different turbulent cases, it was observed that the use of the static ATG led to an increase in the velocity fluctuation ratio. This increase is significant for the transverse component, with the maximum fluctuation ratio increasing from 2.4129 without ATG to 4.0139 with the static ATG. It should be noted for this component that two main neighboring fluctuation areas can be seen near the vortex center in Figure 12b. Given that the maximum value of the ratio is associated with the central value of one of these two bulges, it may be possible that the final maximum value would increase if the two zones were to merge. The difference between the case without ATG and the case with static ATG would then be smaller, and the trend would be more similar to one of the other two components. This hypothesis, however, necessitates further in-depth investigation to fully verify its validity. Moreover, as previously explained, the increase of the fluctuations in the case of the second turbulence case was probably due to the lower wind tunnel flow homogeneity induced by the static ATG. Finally, it is worth noting that increasing the FST led to a decrease in the difference between the velocity fluctuation ratios for the different components. This suggested that the turbulent energy transport was more evenly distributed in all directions, supposedly reflecting an increase in the vortex axis meandering.

6.2. Streamwise swirling strength

The contour maps of the time-averaged streamwise swirling strength for each turbulent case are presented in Figure 15a. The swirling strength (SS) was defined as the product between the vorticity (Ω) and the maximum imaginary part (λ_I) of the eigenvalues of the velocity gradient tensor (Canivete Cuissa & Steiner (2020)), specifically the streamwise swirling strength was computed as:

$$SS_x = \Omega_x \lambda_{Ix}, \qquad \text{with } \Omega_x = \frac{\partial w}{\partial y} - \frac{\partial v}{\partial z} \tag{1}$$

The maximum swirling strength at the center of the vortex was also used to normalize the swirling strength in order to maintain a consistent color scale for all cases. In Figure 15a, the wingtip vortex was identified by a high concentration of swirling strength near the center of the frame which was circular in shape extending up to $r/c = 0.06$ for the no-ATG case, and $r/c = 0.07$ when the ATG in static mode was installed. For the random cases, the concentration extended up to $r/c = 0.15$ for the least turbulent case, and up to $r/c = 0.25$ for the most turbulent one. The maximum values

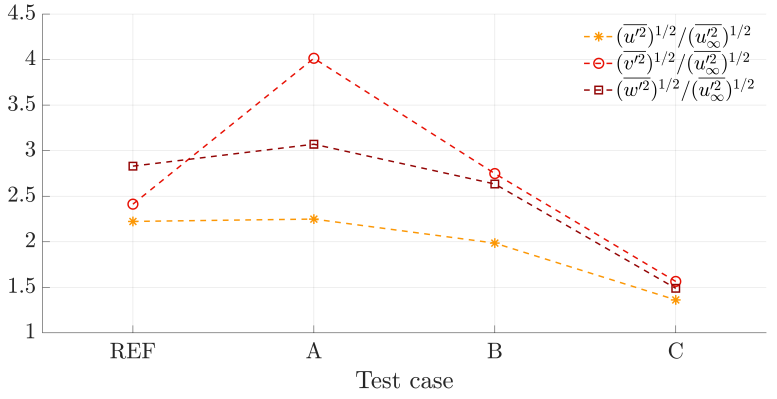

Figure 14: Evolution of the maximum normalized streamwise, transverse, and spanwise velocity fluctuations against the four turbulent cases. (REF) $T_i = 0.2\%$, (A) $T_i = 3\%$, (B) $T_i = 8\%$, and (C) $T_i = 13\%$. Note that the freestream fluctuation rms value vary also with the turbulent case.

of the normalized swirling strength decreased with FST, as shown in Figure 16. The swirling strength contours for the different test cases appeared to grow with increasing FST. The wake shear layer around the vortex concentration area was found to be less intense in swirling strength and increased as the swirling strength diffused with increasing FST. The swirling strength was zero in other regions. However, Figure 15a shows the mean vorticity field, and since the increase of FST leads to an increase of the meandering amplitude according to previous studies (Ben Miloud *et al.* (2020), Pentelow (2014), Bailey & Tavoularis (2008)), the average of the SS over all the frames gives something even more extensive. The average swirling strength field, therefore, did not provide information about the diffusion of the vortex but is an indicator of how the FST affected the meandering of the vortex.

To show the changes in the tip vortex itself caused by FST, the swirling strength data were averaged across the frames after adjusting the instantaneous fields to recenter the vortex at the same location $(\hat{y}, \hat{z}) = (0, 0)$ following the data reduction method in Heyes *et al.* (2004). To identify the center of the vortex in each frame, a non-Galilean invariant approach introduced by Graftieaux *et al.* (2001) was implemented in *Matlab*. This approach consisted in computing the Γ_1 criterion from the SPIV field to extract the position of the vortex center, with $\Gamma_1 \in [0, 1]$ a scalar function defined as

$$\Gamma_1(P) = \frac{1}{N} \sum_S \frac{\left(\boldsymbol{PM} \times \boldsymbol{U}_M\right) \cdot \boldsymbol{e}_x}{|\boldsymbol{PM}|\,|\boldsymbol{U}_M|} = \frac{1}{N} \sum_S \sin\left(\theta_M\right) \tag{2}$$

where S is a two-dimensional area surrounding a fixed point defined by P, where M is a point lying in S, $\boldsymbol{e}_x$ is the unit vector normal to the measurement plane, and θ_M represents the angle between the velocity vector $\boldsymbol{U}_M$ and the radius vector $\boldsymbol{PM}$. When the angles θ_M between the velocity vectors at points M and the radius vector approach $\pi/2$ for a point P, Γ_1 tends towards unity, the maximum value for Γ_1. In practice, Γ_1 rarely reaches unity and the point of maximum Γ_1 is considered as the vortex center. The conditionally averaged swirling strength based on the vortex center $\hat{SS}_x$ was then normalized by its maximum value (all maximum values are provided in Figure 16 and the trend is a general linear decrease of $\hat{SS}_x$, indicating as expected a reduction in vortex strength as FST increased).

The results in Figure 15b indicate that the averaged vortex size, as determined by the vortex core radius, remained fairly constant as FST increased. Furthermore, the SS ratio around the core of the vortex extended slightly, suggesting a diffusion of the vortex with increasing FST. As will be shown in subsection 6.6, there was a slight increase in the average radius of the vortex. This, in conjunction with the decrease in swirling strength indicated in Figure 16, suggested an increase in the diffusion of the vortex with FST, in agreement with Pentelow (2014) and Ben Miloud *et al.* (2020).

6.3. Azimuthal velocity profile

The ensemble average of the vortex azimuthal velocity was evaluated as a function of the radial distance in Figure 17a. The azimuthal velocity was determined by using the velocity components $\overline{v}$ and $\overline{w}$ in the Cartesian

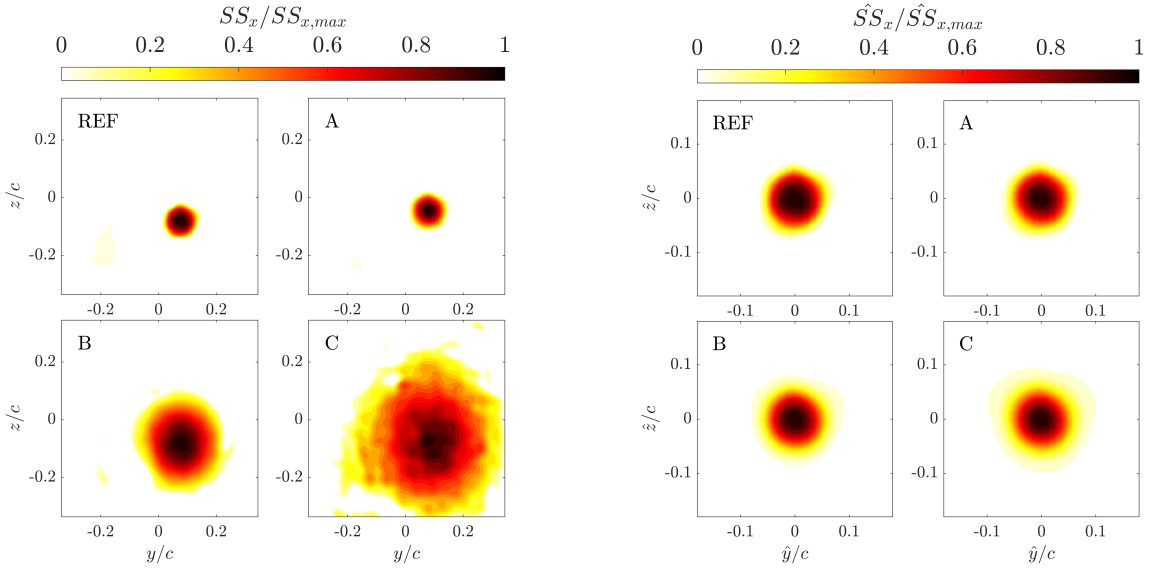

Figure 15: (a) Contours of the normalized averaged streamwise swirling strength, SS_x. (b) Contours of the normalized and conditionally averaged streamwise swirling strength based on the vortex center, $\hat{SS}_x$. Note that the scale of (b) is smaller than (a). (REF) $T_i = 0.2\%$, (A) $T_i = 3\%$, (B) $T_i = 8\%$, and (C) $T_i = 13\%$.

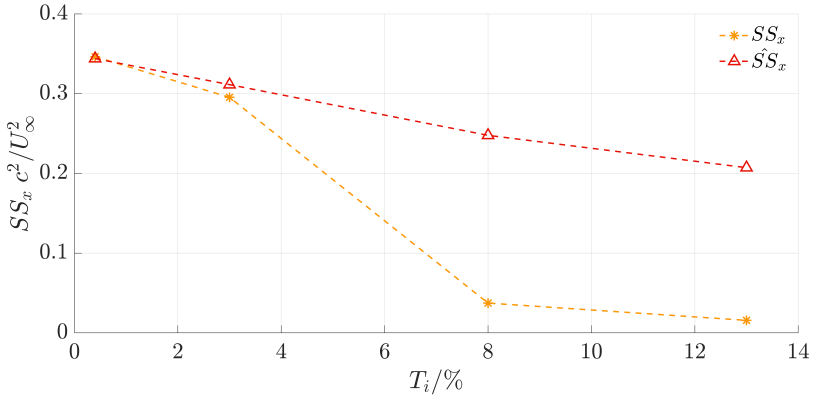

Figure 16: Evolution of the maximum streamwise swirling strength and maximum conditionally averaged streamwise swirling strength based on the vortex center against T_i.

coordinate system and converting them into polar coordinates, as:

$$\overline{u}_\theta = \overline{w}\cos(\theta) - \overline{v}\sin(\theta) \tag{3}$$

This transformation then allowed for the calculation of the azimuthal velocity from the center of the vortex along circular paths divided into 360°, with each degree representing a specific angular position defined by θ. Moreover, the radii of these circles were increased by 1 mm increments, allowing measurement at different distances from the vortex center. The vortex size was characterized by the vortex core radius (radius of maximum azimuthal velocity) defined as r_c. Finally, the velocities laying on a circular path at the same distance from the vortex center were ensemble-averaged to show the evolution of the averaged azimuthal velocity $\langle\overline{u}_\theta\rangle$ along the radial distance.

Figure 17a reveals a clear relationship between the azimuthal velocity peak and FST, with the peak velocity decreasing as FST increased. Therefore, the velocity profiles became gradually flatter as FST increased. This finding

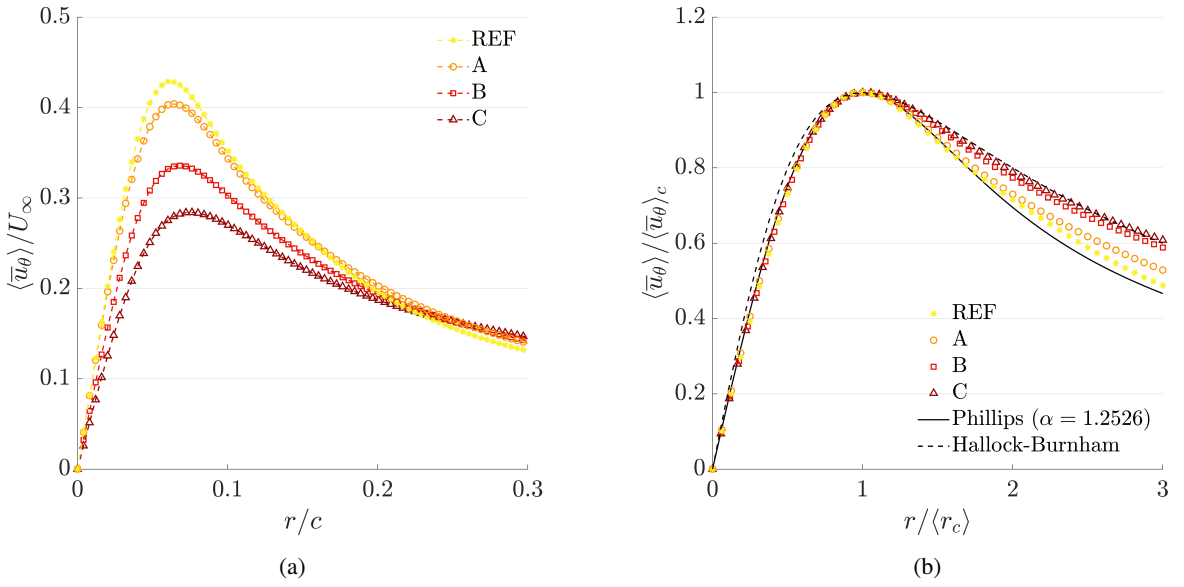

Figure 17: (a) Normalized azimuthal core velocity profiles for each turbulent case. (b) Comparison of the normalized core azimuthal velocity profiles for each turbulent case with the fitting curve of Phillips (Phillips (1981)). (REF) $T_i = 0.2\%$, (A) $T_i = 3\%$, (B) $T_i = 8\%$, and (C) $T_i = 13\%$.

is consistent with the observation that, regardless of the level of turbulence, the azimuthal velocity in the outer core decreased with radial distance after reaching its peak, ultimately asymptotically approaching a constant value, in agreement with the results reported by Bailey *et al.* (2006). Additionally, the observation that the vortex core velocity gently shifted towards higher radii[3] with FST suggested that the vortex size and diffusion increased with FST as mentioned in subsection 6.2. This finding is in agreement with Pentelow (2014), Ghimire & Bailey (2017), and Ben Miloud *et al.* (2020).

Figure 17b shows the evolution of the azimuthal velocity normalized by the azimuthal velocity at the core $\langle \overline{u}_\theta \rangle_c$ as a function of the radial distance normalized by the radius of the vortex core r_c. The experimental curves were compared to the Phillips model (Phillips (1981)) as suggested by Ben Miloud *et al.* (2020) to highlight the self-similarity behavior of the azimuthal velocity profiles:

$$\frac{\langle \overline{u}_\theta \rangle}{\langle \overline{u}_\theta \rangle_c} = \left(1 + \frac{1}{2\beta}\right) \frac{r_c}{r} \left(1 - \exp\left(-\beta \frac{r^2}{r_c^2}\right)\right) \tag{4}$$

where $\beta = 1.2526$ has been chosen to fit with the Lamb-Oseen model (Lamb & Caflisch (1993)). A second comparison model, the Hallock-Burnham model (Burnham & Hallock (1982)) was also used, as suggested in Ghimire & Bailey (2017). The azimuthal velocity profile for this model is defined by:

$$\langle \overline{u}_\theta \rangle = \frac{\Gamma_\infty}{2\pi r} \left(\frac{r^2}{r^2 + r_c^2}\right) \tag{5}$$

where the freestream circulation Γ_∞ was chosen such that $\langle \overline{u}_\theta \rangle = \langle \overline{u}_\theta \rangle_c$ when $r = r_c$. It was observed that both the Phillips and Hallock-Burnham models fit the profiles reasonably well. The Phillips model was also a better fit with the lowest FST cases in the outer core ($r > r_c$). However, as FST increased, the model that fit best in the outer core became the Hallock-Burnham model as can be seen in Figure 17b. These findings are consistent with Ghimire & Bailey (2017). While the profiles in the outer core showed some deviations from the Phillips model, the azimuthal velocity profiles

[3]The increase in radii is here very small but is shown in section 7.

for the experimental data in the inner core region were well-matched with the Phillips model, indicating that the inner core structure of the vortex was self-preserved, as presented by Ben Miloud *et al.* (2020). Misaka *et al.* (2014) showed that the azimuthal velocity profile during the initial vortex roll-up adhered to the Lamb-Oseen vortex model. However, after the completion of the roll-up process, the Hallock-Burnham model provided a more accurate representation of the vortex behavior. Considering that the Phillips model shares similarities with the Lamb-Oseen model, it was inferred that the increase in FST enhanced the speed at which the vortex reached its fully developed structure.

6.4. Vortex circulation

Figure 18 shows the evolution of the circulation $\langle\Gamma\rangle$ normalized by the circulation at the vortex core with the radial distance from the center of the vortex. The circulation was computed along a circular path for each radius r of interest via:

$$\langle\Gamma\rangle(r) = 2\pi r\langle\overline{u}_\theta\rangle(r) \tag{6}$$

For each turbulence condition, the value for the circulation at the vortex core $\langle\Gamma_c\rangle$ was used to normalize the circulation $\langle\Gamma\rangle$. In the inner core ($r/r_c < 1$), the circulation followed a parabolic function of the radius, indicating that the inner core was in approximately rigid-body rotation, as noted by Pentelow (2014). As we increase in normalized radial distance, the circulation increases until it reaches an inflection point at $r/r_c = 1$ beyond which the rate of growth starts to decrease as the vortex velocity field approaches an irrotational state outside the core region (Dghim *et al.* (2018)). Increasing the FST beyond this point also led to a shift in the point where the circulation ratio first starts to decrease. In addition, the circulation ratio increased with FST, indicating possibly a reduction in circulation near the core radius and therefore an increase in vortex diffusion, in agreement with Ghimire & Bailey (2017) and Ben Miloud *et al.* (2020). Both Phillips and Hallock-Burnham models were also plotted to compare to the experimental circulation profiles. It is noteworthy that in the least turbulent case, the Phillips model provided a reasonable fit, while in the most turbulent case, the Hallock-Burnham model was better. This is consistent with the conclusions drawn earlier regarding the azimuthal velocity profiles.

6.5. Axial and radial velocity profiles

The velocity profiles in Figure 19a and Figure 19b show the evolution of the normalized axial velocity and the normalized radial velocity respectively. For the first figure, the axial velocity was determined by interpolating the streamwise velocity from each instantaneous field between the center of the vortex determined using the *Matlab* script implementing the Graftieaux *et al.* (2001) algorithm and a circle of arbitrary radius. The axial velocities where then averaged on circles of increasing radius to have the averaged axial velocity profile plotted against radial distance. For each turbulence case, the velocity deficit decreased with the radial distance and exhibited a flattening and asymptotic evolution for high radii, which is consistent with the findings of Pentelow (2014). However, in the two lower turbulent cases, the normalized axial velocity exceeded unity before following the expected asymptotic behavior. Furthermore, in contrast to Pentelow (2014), the axial velocity deficit within the vortex core appeared to be correlated with increasing FST, with the exception of a discrepancy between the first and second turbulent cases that could be attributed to measurement errors resulting from their close FST proximity. Overall, these findings suggest that the mean velocity field depicted in Figure 11a for the first two turbulent cases may be problematic to determine the axial velocity profiles, as the streamwise velocity deficit deviated from an expected circular symmetry.

In the same way as the azimuthal velocity, the radial velocity was computed by converting the Cartesian velocity components into polar coordinates:

$$\overline{u}_r = \overline{w}\sin(\theta) + \overline{v}\cos(\theta) \tag{7}$$

The radial velocity profiles displayed in Figure 19b exhibited a trend where the velocity initially decreased within the vortex core, which is consistent with Cruz Marquez *et al.* (2021*a*), before increasing again. Moreover, as FST increased, the magnitude of the radial velocity decreased. However, outside of the vortex core, it would have been expected that the average radial velocity of the vortex over a circle of radius r should cancel out, resulting in a profile stabilizing around zero as radial distance increased. This does not appear to be the case here. This discrepancy could be attributed to the central zero line between the two polar regions of Figure 12a and Figure 13a, which was not perfectly straight and could generate deviations from a perfectly zero value when the radial velocities were averaged from the velocities on circles of radii r in these fields. The tendency to diverge from the zero line as radial distance increased was also more pronounced for higher FST, which could be explained by the increased gap between the polar regions in the mean velocity fields with increasing FST.

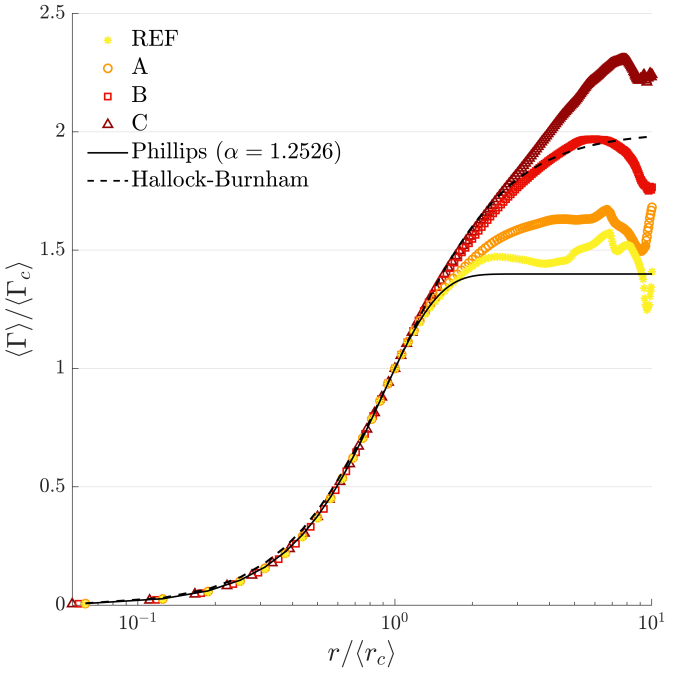

Figure 18: Normalized self-similar vortex circulation profiles for each turbulent case. Comparison with the Phillips model (continuous black line) and the Hallock-Burnham model (dashed black line). (REF) $T_i = 0.2\%$, (A) $T_i = 3\%$, (B) $T_i = 8\%$, and (C) $T_i = 13\%$.

6.6. Probability distributions of vortex characteristics

This part presents an analysis of the vortex characteristics obtained for the whole acquisition data. Probability density distributions were used to show the dispersion of data around their mean, providing information on the probability of the vortex having a certain chance of being located in a particular position. Bailey & Tavoularis (2008) and Van Jaarsveld *et al.* (2011) have previously reported that the meandering amplitude of the vortex increased with FST. Figure 20 presents the 2D probability density distribution of the vortex centers. The darker colors represent the areas where the vortex center was most likely to be located. In the low-turbulent case, the results showed a highly localized vortex center at approximately $(y/c, z/c) \approx (0.08, -0.08)$ that remained stationary for the entire acquisition. This conclusion is reinforced by the scale of the color bar, indicating that the vortex stayed in approximately the same place. For the second turbulent case, the circular concentration area of the probability of the vortex center location started to extend, although it remained fairly localized around $(y/c, z/c) \approx (0.08, -0.08)$. The color bar scale also decreased, indicating the beginning of vortex meandering. In the two most turbulent cases, the probability scales continued to decrease, indicating that fewer vortices were likely to locate at the same place. As FST increased, there was a noticeable increase in the scattering of the vortex positions, in agreement with Bailey & Tavoularis (2008) and Van Jaarsveld *et al.* (2011), indicating an increase in vortex meandering with FST.

Figure 21a displays the evolution of vortex size, defined as the radius of the vortex core r_c, across the acquisition data. The average of these points is marked by the red line. The results showed that the vortex size remained relatively stable for the two least turbulent cases. However, for the second case, the stability decreased slightly with an increase in the deviation from the mean. For the most turbulent cases, the deviation increased again, showing larger and smaller vortices. The average vortex radius is shown in Figure 21b, where a minor increase in average vortex size can be observed. The probability density distribution of vortex size is presented, demonstrating that the proability of having a size close to the mean decreased in favor of larger size as FST increased. The distribution shifted from a Gaussian distribution for the least turbulent case, to a right-skewed distribution with increasing FST, indicating an increase in vortices of larger size. This observation supports the fact that an increase in FST increases the vortex diffusion.

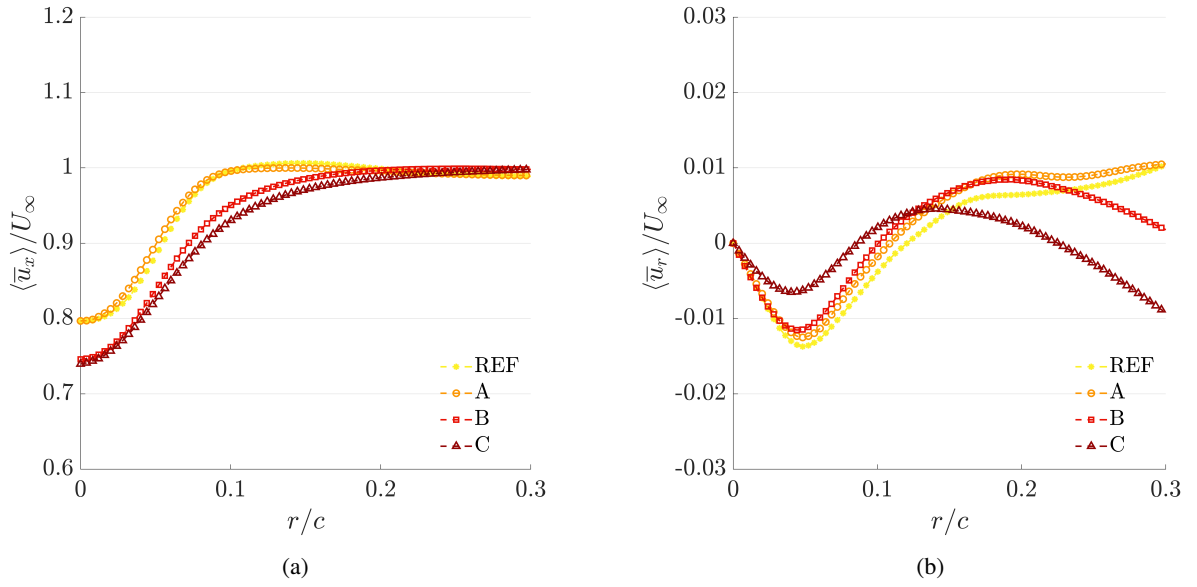

Figure 19: (a) Normalized axial core velocity profiles for each turbulent case. (b) Normalized radial core velocity profile for each turbulent case. (REF) $T_i = 0.2\%$, (A) $T_i = 3\%$, (B) $T_i = 8\%$, and (C) $T_i = 13\%$.

In Figure 22a, time series plots of the core azimuthal velocity with respect to the acquisition data are presented. In conjunction with the information in Figure 21a, it is evident that for the cases with lower turbulence, the maximum azimuthal velocity remained relatively stable around the mean value and followed a normal distribution with mean $\langle \overline{u}_\theta \rangle / U_\infty = 0.4074$ in Figure 22b. As FST increased, the deviation from the mean also increased, resulting in a much larger variation in azimuthal velocities for the most turbulent cases. Additionally, it can be observed that the farthest velocities from the mean in the most turbulent cases were biased towards lower velocities, causing a left-skewed distribution. This effect can be visualized in Figure 22b, where a decrease in the averaged maximum azimuthal velocity can be seen when increasing FST, accompanied with a stretching of the distribution towards lower azimuthal velocities. In the second turbulent case, the average of the maximum azimuthal velocity decreased to $\langle \overline{u}_\theta \rangle / U_\infty = 0.3886$. As for the third and fourth cases, the averages were respectively $\langle \overline{u}_\theta \rangle / U_\infty = 0.3251$, and $\langle \overline{u}_\theta \rangle / U_\infty = 0.2798$. These results complement the results in subsection 6.3 and align with Bailey *et al.* (2006) and Ghimire & Bailey (2017), as the authors also reported a reduction in maximum tangential velocity due to increasing FST.

7. Vortex dynamics and meandering

The following section discusses the dynamics of the vortex and more specifically the phenomenon of vortex meandering, which refers to the low-frequency random motion of the vortex axis in the spanwise-transverse plane.

7.1. Meandering amplitudes

Previous research has extensively documented this phenomenon and its effects on the velocity field statistics (Devenport *et al.* (1996), Heyes *et al.* (2004), Bailey & Tavoularis (2008), Giuni & Green (2013), Ben Miloud *et al.* (2020)). To study the vortex meandering for the wingtip vortices of a NACA-4412 in the different flow conditions, Graftieaux's algorithm (Graftieaux *et al.* (2001)) has been used to identify the instantaneous position of the vortex axis in each frame. Figure 23a shows the path followed by the vortex axis in time. Darker colors correspond to the younger positions of the vortex center. In agreement with the results presented in subsection 6.6, the path remained localized for the low-turbulent case. As FST increased, the path of the vortex axis started to extend into the plane, indicating an increase in meandering.

The position of each vortex axis was recorded and compared to its ensemble-averaged location, which was centered to $(\hat{y}/c, \hat{z}/c) = (0, 0)$. This comparison in Figure 23b revealed an increase in the dispersion of vortex axis positions as the FST increased. The scatter area also became larger with increasing FST. To determine the meandering amplitudes

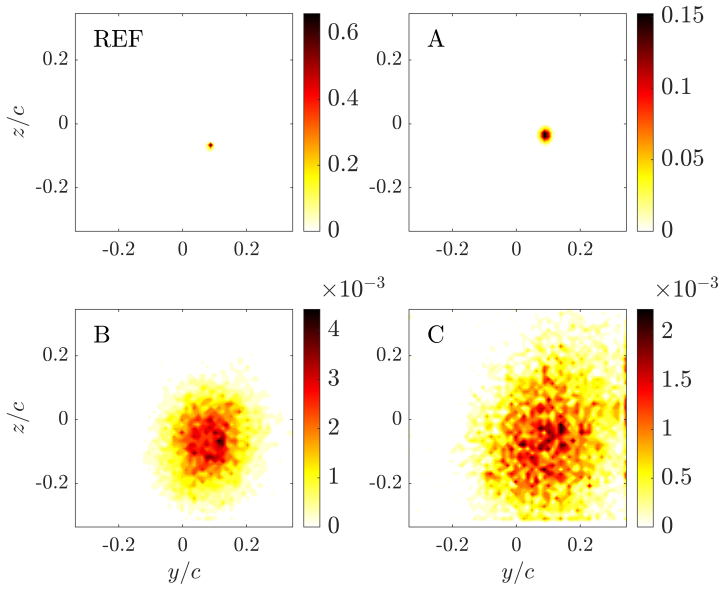

Figure 20: Contours of the probability density function of the vortex position. (REF) $T_i = 0.2\%$, (A) $T_i = 3\%$, (B) $T_i = 8\%$, and (C) $T_i = 13\%$. Note that the scale in the color bars is different.

in the transverse and spanwise directions, denoted σ_y and σ_z respectively, the standard deviations of the time series for the vortex axis displacements from the mean position were calculated for each direction. The evolution of these amplitudes is presented in Figure 24. As expected and noted in Ben Miloud *et al.* (2020) and Bailey *et al.* (2018), the meandering amplitudes strongly increased in both directions with FST.

7.2. Meandering and wing deformation correlation

The relationship between wing deformation and vortex meandering was studied through two scenarios: (i) The correlation between the timeseries of the tip trailing edge displacement and the timeseries of the vortex meandering was studied, with the meandering displacement defined in this case as the distance for each PIV frame in the y-direction of the vortex center from the average of the vortex positions (meandering conditioned). (ii) The correlation between the timeseries of the tip trailing edge displacement and the timeseries of the vortex meandering without conditionally averaging the frames based on the vortex center (meandering unconditioned), measured in the absolute PIV reference frame. Note that, in some frames, the identification of the vortex center using the Γ_1 criterion was not conclusive. Consequently, the amount of information lost in these cases was as follows: 0% for REF and A, 5% for B, and 29% for C. To reduce data loss, a linear interpolation was employed to estimate the isolated non-identified positions of the vortex center in the time series. Subsequently, as many continuous samples of time length 1 s were extracted from the total acquisition time for each specific case. Cross-correlation analysis between tip displacement and vortex displacement for each of those samples was performed individually. To obtain a single representative cross-correlation with a maximum time lag of 1 s, the individual cross-correlation results were finally averaged together. Figure 25a and Figure 25b illustrate the outcome of this process. The cross-correlation coefficients of the two timeseries taken at zero time lag, and the maximum correlation values for both scenarios are gathered in Table 5. For all cases, the zero-lag coefficients were found to be relatively low, suggesting a lack of significant correlation between the wing deformation and the vortex meandering. However, upon examining the magnitude of the maximum coefficients, a general trend emerged indicating an increase in correlation with FST between the low turbulent cases (REF and A) and the highest turbulent cases (B and C). This implied that the displacement of the wing exhibited a greater potential impact on the meandering motion of the vortex axis with higher FST. Moreover, Figure 25a and Figure 25b show a general increase in

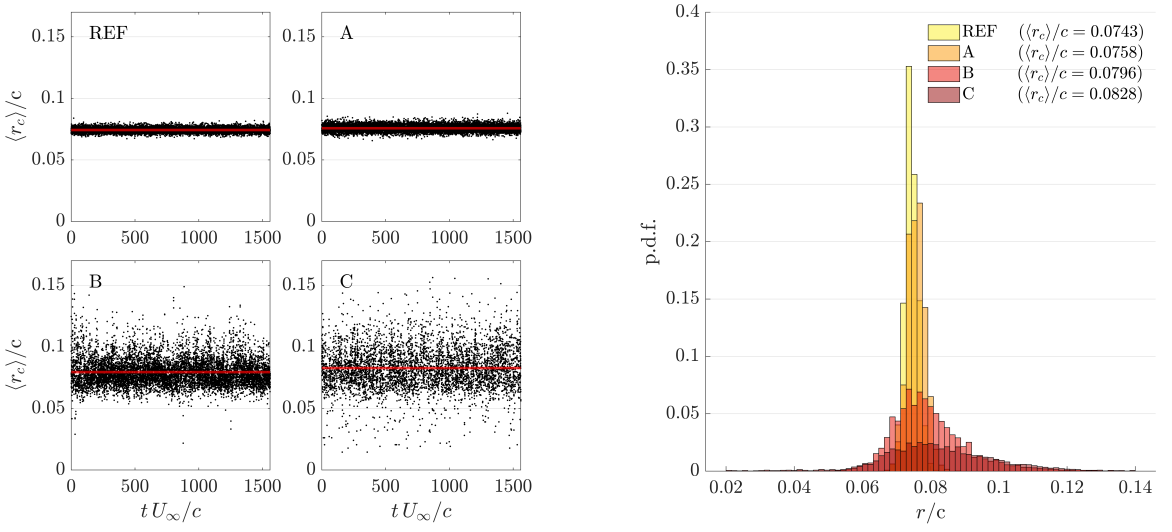

(a) (b)

Figure 21: (a) Evolution of vortex core radius versus normalized time. (b) Probability density function of the vortex size for the 10000 frames. (REF) $T_i = 0.2\%$, (A) $T_i = 3\%$, (B) $T_i = 8\%$, and (C) $T_i = 13\%$.

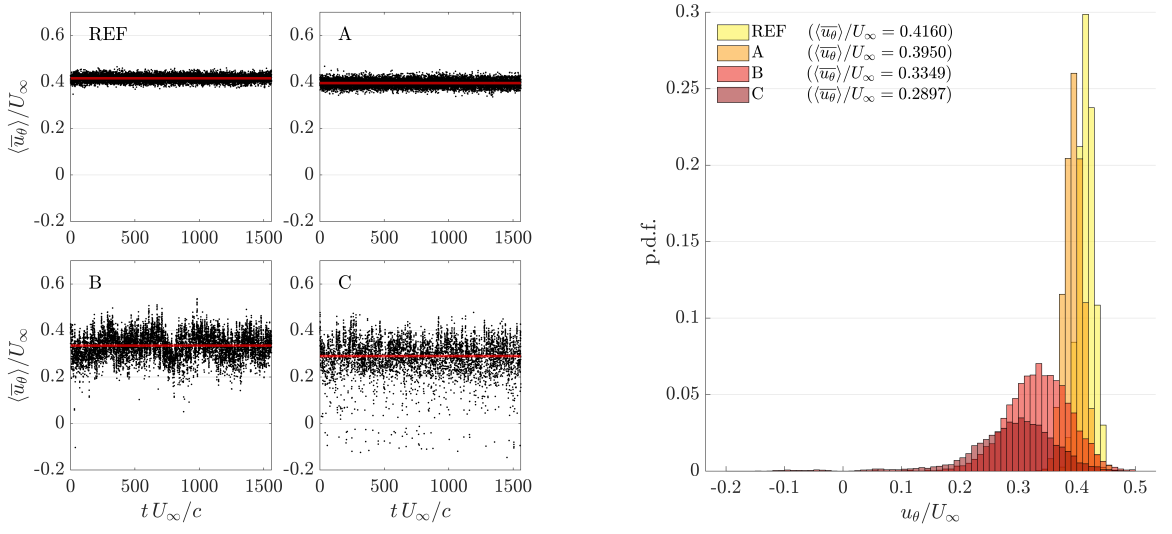

(a) (b)

Figure 22: (a) Evolution of the azimuthal vortex velocity over time. (b) The probability density function of the vortex azimuthal velocity across the 10000 frames. (REF) $T_i = 0.2\%$, (A) $T_i = 3\%$, (B) $T_i = 8\%$, and (C) $T_i = 13\%$.

correlation, where positive and negative correlations display a symmetric-like relationship characterized by anti-peaks. This aligns with expectations, as it suggests that at a specific lag (with a sinusoidal shape due to the back-and-forth motion of the airfoil), there exists either positive or negative correlation of comparable magnitude. Finally, the intensity of this correlation appears to roughly get higher with FST.

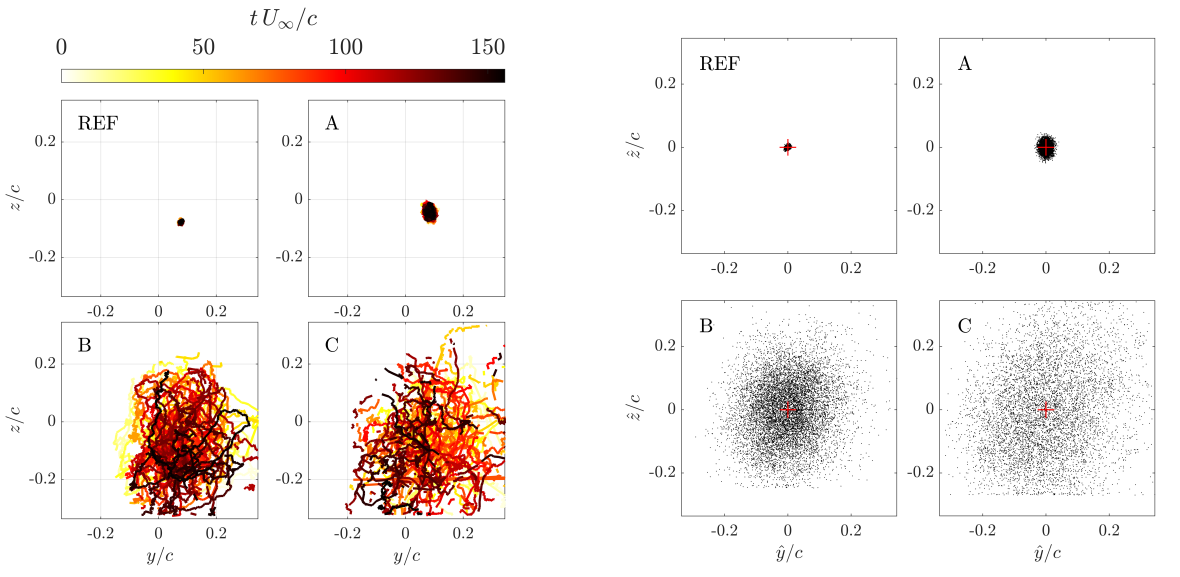

Figure 23: (a) Evolution of vortex center position in time from high-speed acquisition PIV data. The last positions of the vortex center are represented by increasing darkness. The disconnections in the line for the higher two turbulent cases are caused by instantaneous frames where the core could not be detected. (b) Instantaneous vortex center positions for each turbulent case from low-speed acquisition PIV data. The vortex axis (represented by a red cross) was centered on the figure. (REF) $T_i = 0.2\%$, (A) $T_i = 3\%$, (B) $T_i = 8\%$, and (C) $T_i = 13\%$.

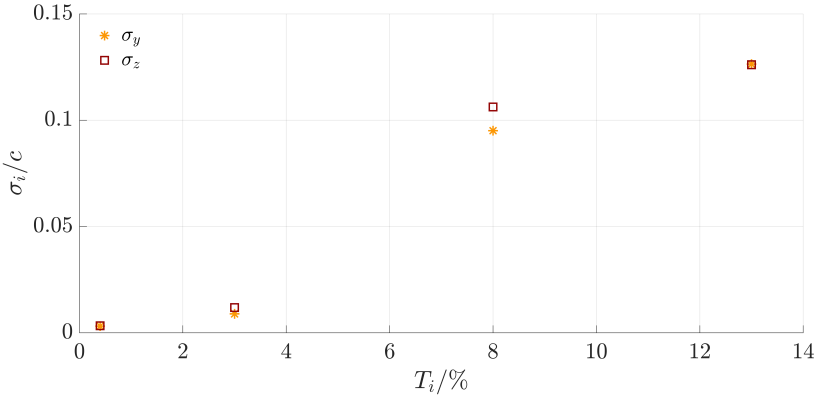

Figure 24: Meandering amplitudes against T_i.

7.3. Meandering spectra

This part aims to investigate the meandering frequency and wavelength to complement the results of the meandering amplitude. The frequency spectra $\phi_{yy}(f)$ and $\phi_{zz}(f)$ were calculated based on vortex core displacement time series in the transverse and spanwise directions respectively, with f the frequency. Two sets of high-speed PIV data were averaged to remove potential noise and a first-order low-pass Butterworth filter was used to reduce the effects of short-wavelength meandering. Only the meandering spectra associated with the transverse direction $\phi_{yy}(f)$ were studied since the spectra in both directions were virtually identical. Indeed, it can be seen in Figure 26a and Figure 26b that the general behavior of the probability distribution of the displacements appeared to be highly similar, despite some differences. Additionally, these probability density functions confirm the findings of Devenport *et al.* (1996) and Heyes *et al.* (2004), who reported that the distribution of vortex axis locations can be approximated by a Gaussian function.

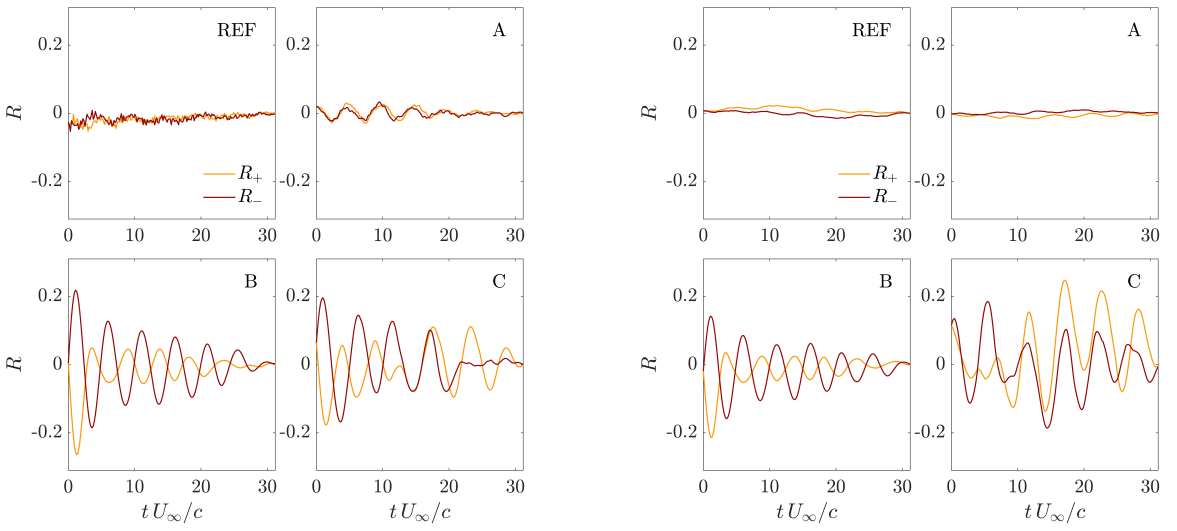

Figure 25: (a) Averaged cross-correlation over 1 s samples for meandering conditioned case. (b) Averaged cross-correlation over 1 s samples for meandering unconditioned case. R_+ corresponds to the cross-correlation coefficients associated with positive time lags, while R_- corresponds to the ones associated with negative time lags. (REF) $T_i = 0.2\%$, (A) $T_i = 3\%$, (B) $T_i = 8\%$, (C) $T_i = 13\%$.

Table 5
Correlation coefficients for zero time lag $R_{0-\text{lag}}$ and maximum correlation coefficients in magnitude R_{max} from the cross-correlation between wingtip trailing edge displacement and vortex meandering motion. The number in brackets indicates the time-lag in ms at which the coefficient has been measured. (REF) $T_i = 0.2\%$, (A) $T_i = 3\%$, (B) $T_i = 8\%$, (C) $T_i = 13\%$.

	Meandering conditioned				Meandering unconditioned			
	REF	A	B	C	REF	A	B	C
$R_{0-\text{lag}}$	−0.026	0.019	0.004	0.064	0.008	−0.002	−0.019	0.115
R_{max}	0.053 (10)	0.033 (301)	0.264 (40)	0.196 (30)	0.023 (357)	0.026 (17.9)	0.214 (40)	0.248 (548)

The frequency spectra, normalized by the core radius for each turbulent case, are shown in Figure 27a. The colored dashed line represents the frequency of the spectrum's highest peak in Figure 27b. The first figure shows that, for the low-turbulent case, the normalized frequency spectrum remained nearly constant in the beginning until reaching $fr_c/U_\infty \approx 0.002$, where it began to decrease for the first time. This was followed by several frequencies for which the spectrum remained constant until $fr_c/U_\infty \approx 0.012$, after which the spectrum decreased again. Similarly, at $fr_c/U_\infty \approx 0.044$, the spectrum decreased for a third time, and finally at $fr_c/U_\infty \approx 0.637$, the spectrum decreased monotonically for a final time. These decreases are associated with the local peaks that can be observed at the same frequencies in Figure 27b. Similar behavior was observed for the other cases as FST increased. In the static-ATG case, the spectrum remained relatively constant and then decreased from $fr_c/U_\infty \approx 0.058$ before reaching an inflection point, from which the spectrum decreased again. This pattern repeated for the highest turbulent cases, except for a small bump before the decrease in the first random ATG case. Moreover, the inflection points in both random ATG cases no longer appeared as the local peaks for these cases in Figure 27b also disappeared. One final observation in Figure 27a is associated with the behavior of the spectrum with respect to FST. It is evident that as FST increased, the spectrum was shifted upwards, indicating a corresponding increase in the energy contained in each frequency. This observation confirms that the meandering motion is composed of very different scales depending on freestream conditions, in agreement with Bailey *et al.* (2018).

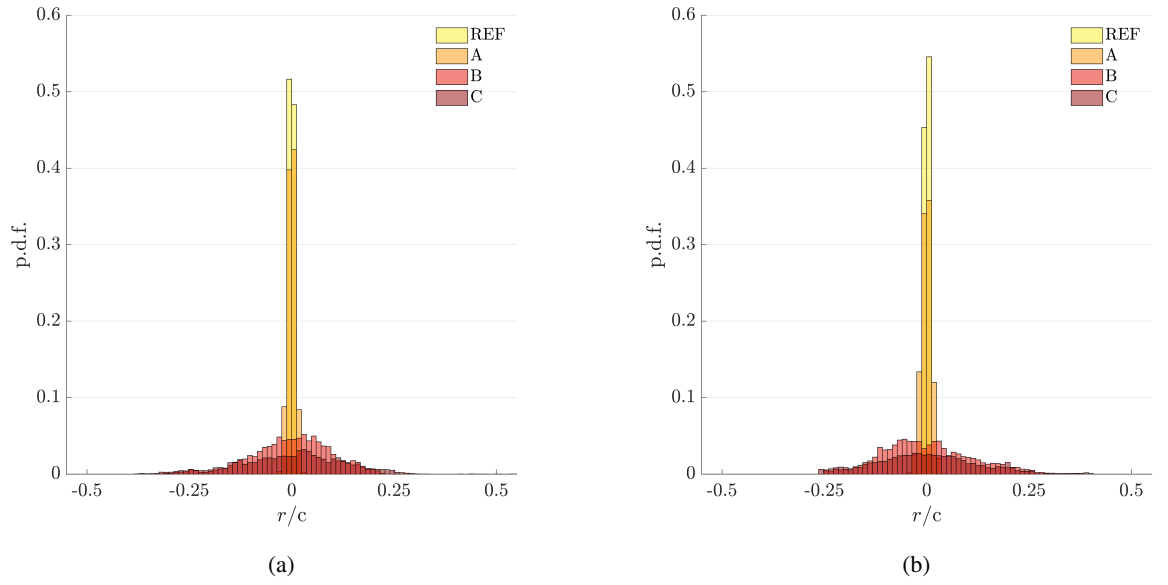

Figure 26: (a) Probability density function of the displacement of the vortex axis from the averaged axis center along y-direction. (b) Same for the z-direction.

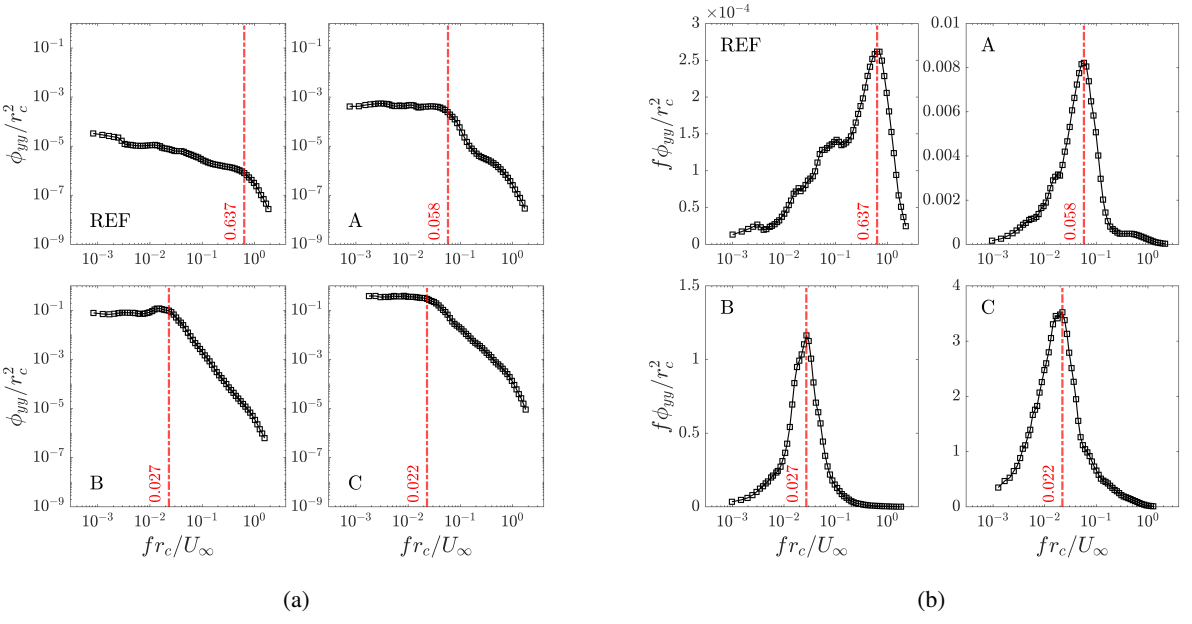

Figure 27: (a) Frequency spectra of meandering amplitude σ_{yy}. (b) Frequency spectra of meandering amplitude σ_{yy} in pre-multiplied form. (REF) $T_i = 0.2\%$, (A) $T_i = 3\%$, (B) $T_i = 8\%$, and (C) $T_i = 13\%$.

In Figure 27b, the ensemble-averaged spectra normalized by the core radius are presented for each turbulence case, using the form suggested in Bailey *et al.* (2018). This form enables a visual comparison of the relatives energies $\sigma_y^2 = \int_0^\infty \phi_{yy} \mathrm{d}f$ and $\sigma_z^2 = \int_0^\infty \phi_{zz} \mathrm{d}f$ between each turbulence case, as the area under the curve is proportional to the relative energy. Additionally, assuming that the vortex was transported by the flow's local freestream velocity U_∞, each frequency that characterized the vortex axis meandering was associated with a wavelength $\lambda_m \approx U_\infty / f$. In the low-turbulence case, the frequency spectrum exhibited a frequency band centered around a peak at $fr_c/U_\infty \approx 0.637$

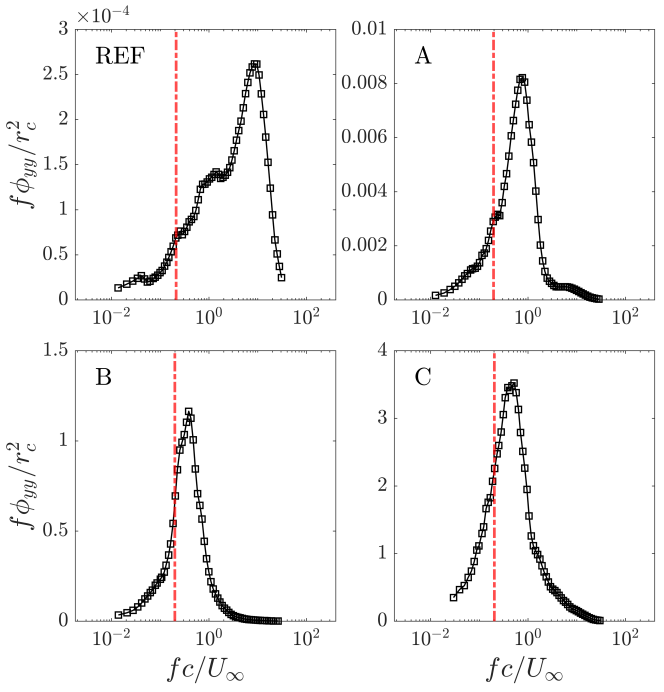

Figure 28: Frequency spectra of meandering amplitude σ_{yy} in pre-multiplied form against frequency normalized by chord length c. (REF) $T_i = 0.2\%$, (A) $T_i = 3\%$, (B) $T_i = 8\%$, and (C) $T_i = 13\%$. The red dashed line represents the 6.2 Hz line.

standing out from other several smaller other local peaks. The frequency band of this peak corresponded to relatively short wavelengths $1 < \lambda_m/r_c < 10$. The three other previously identified local peaks were located in frequency bands corresponding to longer wavelengths $10 < \lambda_m/r_c < 1000$. The area under the curve associated with the shortest wavelengths represented approximately half of the total area, with the other half being associated with longer wavelengths. This result is consistent with Bailey *et al.* (2018), showing that short-wavelength meandering was possibly induced by the interaction between residual turbulence, which arose from small-scale fluctuations, and secondary structures on the wing surface, which may further have amplified the instability in the flow.

As FST increased, the meandering energy extended over several orders of magnitude as it can be noted by the y-axis scale in Figure 27b, demonstrating that the meandering here was composed of displacements at very different scales as FST increased. Between the least (REF) and most turbulent (C) cases, the energy had a difference of four orders of magnitude. The frequency spectra shapes of the cases using the ATG were mainly consistent with one of the low-turbulent cases. A general peak covering a certain frequency band was observed but as FST increased the frequency band associated with this peak expanded as the energy associated with short-wavelength motions decreased in favor of longer wavelengths. In the second case, the peak associated with shorter wavelengths was still detectable but much less significant that in the low-turbulent case, suggesting that some of the energy of short-wavelength motions persisted even when the flow was subject to grid turbulence. As the FST increased, the smaller peak decreased until only the main peak ($10 < \lambda_m/r_c < 100$) remained. In this case, the turbulence generated by the random motion of the ATG eliminated the vast majority of the energy associated with short-wavelength motions.

Figure 27b was then redrawn with a common x-axis by normalizing the frequency by the chord length. In Figure 28, it is evident that the peak associated with the meandering motion does not align with the natural vibration frequency of the wing, which is represented by the red dashed line at 6.2 Hz. Nevertheless, it appears that for the test cases involving the lowest levels of FST (REF and A), there is a minor peak rise at the 6.2 Hz frequency, potentially suggesting a correlation between this particular frequency and the meandering motion in these cases.

8. Conclusions

This study investigated the impact of freestream turbulence (FST) generated by an active turbulence grid (ATG) on the behavior of a wingtip vortex in the near wake of a NACA-4412 and on its aerodynamic performance using several experimental methods. Experimental investigations were conducted in a large-scale closed-loop wind tunnel with four different inflow conditions: a reference case without a grid ($T_i = 0.2\%$), a second case with a static grid ($T_i = 3\%$), and two random ATG cases ($T_i = 8\%$ and $T_i = 13\%$), at a chord-based Reynolds number $Re_c = 1.4 \times 10^5$.

Initially, hot-wire anemometry was used to examine the primary flow characteristics, revealing that the flow homogeneity increased with the random ATG cases, in agreement with Hearst & Lavoie (2015), while the static grid case exhibited relatively poor homogeneity. Force balance measurements were then employed to analyze lift and drag curves with increasing FST. The overall result is an enhancement of the wing aerodynamic performance, with a slight increase in maximum lift and delayed stall observed for higher FST. Furthermore, digital image correlation (DIC) measurements were performed to investigate the deflection of the wing. The first two Proper Orthogonal Decomposition (POD) modes were investigated. It revealed that the majority of the wing motion energy was attributed to two deflection motions, spanwise bending, and mid-chord twist. Stereo Particle Image Velocimetry (SPIV) measurements were conducted to quantitatively assess the flow field at a distance of $2c$ downstream of the trailing edge, and to investigate the meandering behavior of the vortex axis. Overall, the vortex core exhibited wake-like characteristics and displayed an axial velocity deficit compared to the freestream velocity, with the magnitude of the deficit decreasing with increasing FST. The velocity fluctuation ratio also decreased with FST, indicating an enhanced distribution of energy transport in all directions, testifying to an increase in the vortex axis meandering. The meandering correction analysis in the vorticity field demonstrated a reduction in vortex strength with increasing FST, along with a slight increase in diffusion. Additionally, the maximum azimuthal velocity generally decreased with higher FST values, while the core radius of the vortex was pushed towards slightly higher radii. Model fitting analysis revealed that the Phillips model provided a better fit for low FST cases, whereas the Hallock-Burnham model exhibited better agreement in the outer core for larger FST cases. Similarly, the circulation of the vortex aligned more closely with the Phillips model for low FST cases, while the Hallock-Burnham model was more suitable for higher FST cases. FST also had a significant impact on increasing meandering amplitude and the energy associated with meandering motion at longer wavelengths, at the expense of energy contained in shorter wavelength motions. Finally, the correlation between wing deformation and vortex meandering was investigated. The analysis revealed that, while the zero-lag coefficients were relatively low across all test cases, a trend emerged. The maximum coefficients indicated an increase in correlation with higher FST, implying that the wing displacement had a more significant influence on vortex meandering under higher FST. Additionally, positive and negative correlations exhibited a symmetric-like relationship characterized by anti-peaks, indicating comparable magnitudes of correlation at specific lags.

Future research directions can build upon the findings of this work and explore various aspects related to the performance of the wing. Some potential areas for further investigation include examining the influence of 3D effects on wing performance, conducting SPIV measurements at several downstream positions to gain insights into the wingtip vortex development, and exploring the impact of different Reynolds numbers. Moreover, a deeper investigation into the meandering behavior can be pursued as this aspect still represents a considerable gap in the global knowledge in this field of research.

References

Ahmadi-Baloutaki, M., Carriveau, R. & Ting, D. 2014 Frequency analysis of a trailing vortex flow subjected to external turbulence. *ASME International Mechanical Engineering Congress and Exposition, Proceedings (IMECE)* **1**, Montreal, Quebec, Canada. V001T01A004.

Bailey, S., Pentelow, S., Ghimire, H., Estejab, B., Green, M. & Tavoularis, S. 2018 Experimental investigation of the scaling of vortex wandering in turbulent surroundings. *Journal of Fluid Mechanics* **843**, 722–747.

Bailey, S. & Tavoularis, S. 2008 Measurements of the velocity field of a wing-tip vortex, wandering in grid turbulence. *Journal of Fluid Mechanics* **601**, 281–315.

Bailey, S., Tavoularis, S. & Lee, B. 2006 Effects of free-stream turbulence on wing-tip vortex formation and near field. *Journal of Aircraft* **43** (5), 1282–1291.

Baldwin, B. & Barth, T. 1991 A one-equation turbulence transport model for high reynolds number wall-bounded flows. *29th Aerospace Sciences Meeting* pp. AIAA 1991–610.

Ben Miloud, K., Dghim, M., Fellouah, H. & Ferchichi, M. 2020 Free-stream turbulence interaction with a wing-tip vortex. *Journal of Wind Engineering and Industrial Aerodynamics* **206**, 104211.

Benedict, L. & Gould, R. 1996 Towards better uncertainty estimates for turbulence statistics. *Experiments in Fluids* **22** (2), 129–136.

Burnham, D. C. & Hallock, J. N. 1982 Chicago monostatic acoustic vortex sensing system : Vol. iv. wake vortex decay pp. Report No. DOT/FAA/RD–79–103, IV, United States. Federal Aviation Administration.

Bölle, T., Brion, V., Couliou, M. & Molton, P. 2023 Experiment on jet–vortex interaction for variable mutual spacing. *Physics of Fluids* **35** (1), 015117.

Canivete Cuissa, J. R. & Steiner, O. 2020 Vortices evolution in the solar atmosphere - a dynamical equation for the swirling strength. *Astronomy & Astrophysics* **639** (A118).

Chow, J.S., Zilliac, G.G. & Bradshaw, P. 1997 Mean and turbulence measurements in the near field of a wingtip vortex. *AIAA Journal* **35** (10), 1561–1567.

Craft, T.J., Launder, B.E. & Robinson, C.M.E. 2005 The computational modelling of wing-tip vortices and their near-field decay. *Engineering Turbulence Modelling and Experiments* **6**, 627–636.

Cruz Marquez, R., Monnier, J.C., Tanguy, G., Couliou, M., Brion, V., Cattafesta, L. & Dupont, P. 2021*a* An experimental study of a trailing vortex alleviation using an undulated trailing edge. *AIAA Aviation forum 2021-2562* p. Session: Vortical/Vortex Flow Aerodynamics.

Cruz Marquez, R., Monnier, J.C., Tanguy, G., Couliou, M., Brion, V. & Dupont, P. 2021*b* An experimental study of trailing vortex dynamics on cruise and high-lift wing configurations. *AIAA Aviation forum 2022-3390* p. Session: Vortical/Vortex Aerodynamics II.

Dacles-Mariani, J., Zilliac, G.G., Chow, J.S. & Bradshaw, P. 1997 Numerical/experimental study of a wingtip vortex in the near field. *AIAA Journal* **33** (9), 1561–1568.

Devenport, W., Rife, M., Liapis, S. & Follin, G. 1996 The structure and development of a wing-tip vortex. *Journal of Fluid Mechanics* **312**, 67–106.

Dghim, M., Ferchichi, M. & Fellouah, H. 2018 Mid-wake wing tip vortex dynamics with active flow control. *Experimental Thermal and Fluid Science* **98**, 38–55.

Gerz, T., Holzäpfel, F. & Darracq, D. 2002 Commercial aircraft wake vortices. *Progress in Aerospace Sciences* **38** (3), 181–208.

Ghimire, H. & Bailey, S. 2017 An experimental investigation of wing-tip vortex decay in turbulence. *Physics of Fluids* **29** (3), 037108.

Giuni, M. & Green, R.B. 2013 Vortex formation on squared and rounded tip. *Aerospace Science and Technology* **29** (1), 191–199.

Graftieaux, L., Michard, M. & Grosjean, N. 2001 Combining piv, pod and vortex identification algorithms for the study of unsteady turbulent swirling flows. *Measurement Science and Technology* **12** (9), 1422.

Green, S. & Acosta, A. 1991 Unsteady flow in trailing vortices. *Journal of Fluid Mechanics* **227**, 107–134.

Hearst, R.J. & Lavoie, P. 2015 The effect of active grid initial conditions on high reynolds number turbulence. *Experiments in Fluids* **56** (185).

Heyes, A. L., Jones, R. F. & Smith, D. A. R. 2004 Wandering of wing-tip vortices. *Proceedings of the 12th International Symposium on Applications of Laser Techniques to Fluid Mechanics* pp. Lisbon, Portugal, Paper 35–3.

Hoffmann, J.A. 1991 Effects of freestream turbulence on the performance characteristics of an airfoil. *AIAA Journal* **29** (9).

Hultmark, M. & Smits, A.J. 2010 Temperature corrections for constant temperature and constant current hot-wire anemometers. *Measurement Science and Technology* **21**, 105404.

Kay, N.J., Richards, P.J. & Sharma, R.N. 2020 Influence of turbulence on cambered and symmetrical airfoils at low reynolds numbers. *AIAA Journal* **58** (5), 1913–1925.

Kildal, O., Li, L., Hearst, R.J., Petersen, Ø.W. & Øiseth, O. 2020 On the use of an active turbulence grid in wind tunnel testing of bridge decks. *Journal of Wind Engineering and Industrial Aerodynamics* **233**, 105331.

Lamb, H. & Caflisch, R. 1993 Hydrodynamics. *Cambridge University Press* pp. ISBN: 0521458684, 9780521458689.

Larssen, J.V. & Devenport, W.J. 2011 On the generation of large-scale homogeneous turbulence. *Experiments in Fluids* **50**, 1207–1223.

Li, L. & Hearst, R.J. 2021 The influence of freestream turbulence on the temporal pressure distribution and lift of an airfoil. *Journal of Wind Engineering and Industrial Aerodynamics* **209**, 104456.

Lien, F.S. & Leschziner, M.A. 1994 A general non-orthogonal collocated finite volume algorithm for turbulent flow at all speeds incorporating second-moment turbulence-transport closure, part 1: Computational implementation. *Computer Methods in Applied Mechanics and Engineering* **114** (1-2), 123–148.

Misaka, T., Obayashi, S., Stephan, A., Holzäpfel, F. N., Gerz, T. & Nakahashi, K. 2014 Numerical simulation of jet-wake vortex interaction. *52nd Aerospace Sciences Meeting* pp. AIAA 2014–0926.

Moore, D.W., Saffman, P.G. & Stewartson, K. 1973 Axial flow in laminar trailing vortices. *Proceedings of the Royal Society of London. A. Mathematical and Physical Sciences* **333**, 491–508.

Mueller, T., Pohlen, L., Conigliaro, P. & Jansen Jr., B. 1983 The influence of free-stream disturbances on low reynolds number airfoil experiments. *Experiments in Fluids* **1**, 3–14.

O'Regan, M., Griffin, P. & Young, T. 2013 Wingtip vortices in the near-field – a numerical and experimental investigation. *4th CEAS Air & Space Conference, FTF Congress: Flygteknik* .

Pentelow, S. 2014 Wing-tip vortex structure and wandering pp. Ph.D. thesis, Université d'Ottawa.

Phillips, W.R.C. 1981 The turbulent trailing vortex during roll-up. *Journal of Fluid Mechanics* **105**, 451–467.

del Pino, C., Parras, L., Felli, M. & Fernandez-Feria, R. 2011 Structure of trailing vortices: Comparison between particle image velocimetry measurements and theoretical models. *Physics of Fluids* **23** (1), 013602.

Raffel, M., Willert, C.E., Scarano, F., Kähler, C.J., Wereley, S.T. & Kompenhans, J. 2018 Particle image velocimetry: A practical guide pp. 3rd ed., Springer, Switzerland.

Reddy, S., Dulikravich, G., Sobieczky, H. & Gonzale, M. 2019 Bladelets—winglets on blades of wind turbines: A multiobjective design optimization study. *Journal of Solar Energy Engineering* **141** (6), 061003.

Rogers, S.E., Kwak, D. & Kiris, C. 1991 Steady and unsteady solutions of the incompressible navier-stokes equations. *AIAA Journal* **29** (4), 603–610.

Sarpkaya, T. & Daly, J.J. 1987 Effect of ambient turbulence on trailing vortices. *Journal of Aircraft* **24** (6), 309–404.

Sciacchitano, A. & Wieneke, B. 2016 Piv uncertainty propagation. *Measurement Science and Technology* **27**, 084006.

SERRANO-AGUILERA, J., GARCÍA-ORTIZ, J., GALLARDO-CLAROS, A., PARRAS, L. & DEL PINO, C. 2016 Experimental characterization of wingtip vortices in the near field using smoke flow visualizations. *Experiments in Fluids* **57** (137).

SPALL, R.E. 2001 Numerical study of a wing-tip vortex using the euler equations. *Journal of Aircraft* **38** (1), 22–27.

SWALWELL, K., SHERIDAN, J. & MELBOURNE, W. 2001 The effect of turbulence intensity on stall of the naca 0021 aerofoil. *14th Australasian Fluid Mechanics Conference* pp. Adelaide University, Adelaide, Australia.

VAN JAARSVELD, J.P.J., HOLTEN, A.P.C., ELSENAAR, A., TRIELING, R.R. & VAN HEIJST, G.J.F. 2011 An experimental study of the effect of external turbulence on the decay of a single vortex and a vortex pair. *Journal of Fluid Mechanics* **670**, 214–239.

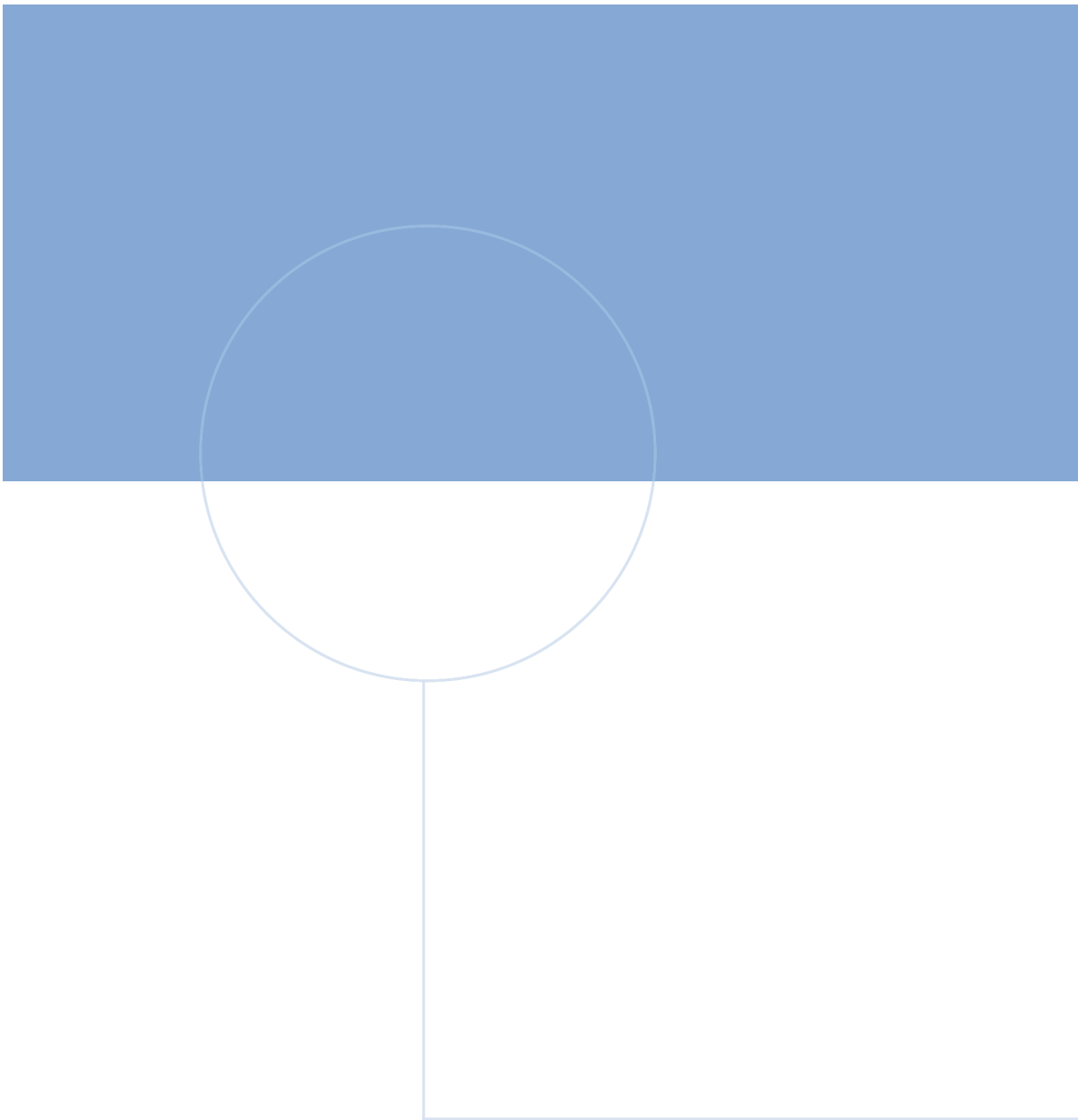

NTNU

Norwegian University of
Science and Technology